CHALMERS

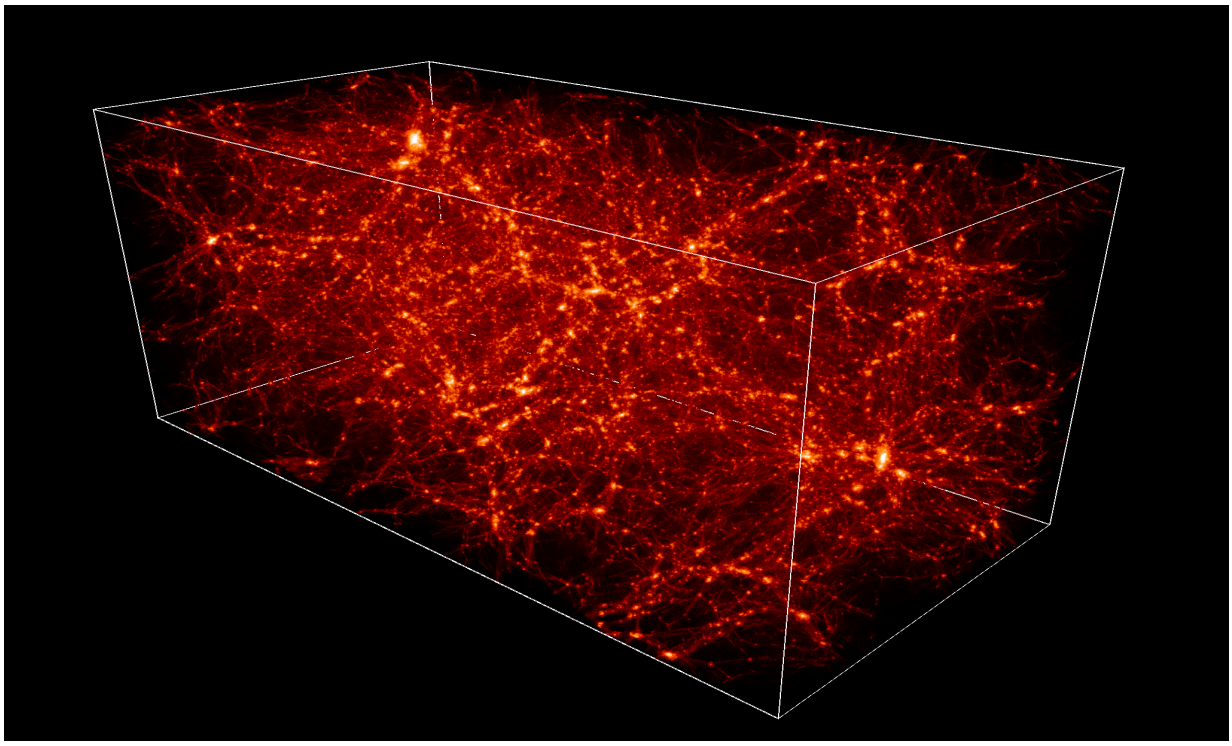

Simulations of Structure Formation in the Universe: Hot vs Cold Dark Matter

Master's Thesis in Radio and Space Science

CARLOS CHOVER LóPEZ

Supervisor: Alessandro Romeo

Department of Radio and Space Science
CHALMERS UNIVERSITY OF TECHNOLOGY
Göteborg, Sweden 2010
Master's Thesis 2010:03

MASTER'S THESIS 2010:03

Simulations of Structure Formation in the Universe: Hot vs Cold Dark Matter

Master's Thesis in Radio and Space Science

CARLOS CHOVER LóPEZ

Supervisor: Alessandro Romeo

Department of Radio and Space Science
CHALMERS UNIVERSITY OF TECHNOLOGY

Göteborg, Sweden 2010

Simulations of Structure Formation in the Universe: Hot vs Cold Dark Matter
CARLOS CHOVER LóPEZ

©CARLOS CHOVER LóPEZ, 2010

Master's Thesis 2010:03
Department of Radio and Space Science
Chalmers University of Technology
SE-412 80 Göteborg
Sweden
Telephone: + 46 (0)76-583 8813

Cover:
Dark matter simulation
(Pichon et al., MNRAS, 2001, 326, 597)

Chalmers Reproservice
Göteborg, Sweden 2010

Simulations of Structure Formation in the Universe: Hot vs Cold Dark Matter
Master's Thesis in Radio and Space Science
CARLOS CHOVER LóPEZ
Department of Radio and Space Science
Chalmers University of Technology

Abstract

In the last century, new observational techniques and discoveries such as the Cosmic Microwave Background Radiation have brought a new dimension of knowledge about the Universe. Therefore new theories and models have been proposed to explain the observed Universe. Computer simulations are a very important tool because they lay a bridge between theory, often over-simplified, and observations, which reveal the complexity of our Universe.

In this thesis, it is given a review of observations including the most important discoveries and results that help to describe the Universe and have been used to develop the models considered nowadays. The cosmological theory behind the large-scale structure formation is explained, from the basis of the Friedman model to the formation of structures through the linear, quasi-linear and non-linear regime, including the Zeldovich approximation and the spherical collapse model. Furthermore, the different types of codes used for cosmological simulations are introduced, focusing on the N-body codes and presenting the code used in this thesis, developed by Klypin & Holtzman (1997). The tools used to analyse the results: density plots, power spectrum and mass variance are described as well.

Three main sets of simulations have been performed: a basic simulation (RUN0) with standard cosmological parameters, simulations of ΛCDM and simulations of Hot+Cold Dark Matter (HCDM). All the simulations use 32^3 particles, while different cosmological parameters have been changed e.g. σ_8, Ω_m, Ω_Λ and n. Thus, it is observed that higher values of Ω_m and low values of Ω_Λ lead to more clustering and hence more developed structures. Moreover, the effect of σ_8 appears to be critical, since it determines the amplitude of the density fluctuations at the initial redshift of the simulation. When studying the presence of hot dark matter, the main difference comes from the cut-off in the power spectrum due to the hot dark matter free-streaming, resulting in less developed structures. Similarly to the previous case, the effects of the cosmological parameters are explained for this model.

Finally, some additional simulations regarding dark halos populations and density profiles are included in the Appendix.

Keywords: Cosmology, Cold Dark Matter, Hot Dark Matter, N-body, Simulation

Contents

Preface

In this thesis different N- body simulations have been performed in order to study the effects of different cosmological parameters, as well as the presence of hot dark matter in the Universe.

The work has been carried out from January 2010 to June 2010 at the Department of Radio and Space Science, Chalmers University of Technology, Sweden, with Carlos Chover López as student and Alessandro Romeo as supervisor.

Aknowledgements

I would like to say thanks to my supervisor Alessandro Romeo for his support and help, to the master program coordinator Arto Heikkilä, and to the other master thesis students at the department, who have helped me in this project. Without their help this project would not have been possible.

Göteborg June 2010
Carlos Chover López

Chapter 1

Introduction

1.1 Motivation

The formation of large-scale structures and how the Universe has developed until the present state are issues discussed and studied since the beginning of the 20th century. Since then, many theories have appeared trying to solve these problems, however it has been in the second part of the century, and especially since the 80s when our knowledge of the Universe has started to become more precise.

Thus, the presence of dark matter has needed a long time to be widely accepted by the scientific community. This concept was firstly introduced by Fritz Zwicky in 1933 and states that there is a type of matter, which cannot be detected directly using the actual technology, that interacts with the "normal" matter through gravitation. Zwicky noticed that the velocity of galaxies in large clusters was too great to maintain gravitational stability, hence there should be a mass contribution from an unknown source. Needless to say dark matter was a very controversial issue when it was presented, and it required many years to start to be accepted. Furthermore, the elements forming dark matter are unknown, being possible to classify the candidates in two main groups: cold dark matter and hot dark matter (e.g. Primack & Gross 2000). Each type has different origin and characteristics, and since it is not exactly understood the proportion of each component in the Universe, this field is still a hot topic in cosmology.

Another element considered nowadays to explain the observed Universe is the dark energy, which can be understood as a negative force that enhances the expansion of the Universe. Dark energy has been studied since some observations discovered that the expansion rate of the Universe is increasing, as seen by the Supernovae Ia observations (e.g. Riess 2000). Again, many discussions and studies have been needed to reach an agreement about this field, since the nature of dark energy, as well as dark matter, are still unknown.

These two concepts are examples of how the knowledge about the Universe has changed in recent times, and how is still evolving. Nevertheless, the new theories and ideas that are continuously being presented need observations to validate them. Fortunately, the observational tools have been improving continuously, leading to what is known as the actual "precision cosmology", where the cosmological parameters defining the Universe are being determined with a high degree of detail. This is due to the fact that new discoveries and surveys have allowed to observe the current and the very young Universe. Thus, the

young Universe is studied using the Cosmic Microwave Background Radiation, detected by e.g. the COBE and the WMAP satellites (Bennet et al. 1993; Jarosik et al. 2010), while the current distribution of the Universe is observed with telescopes and radio-telescopes in projects such as the new generation of galaxies surveys: the 2-degree Field Galaxy Redshift Survey, or 2dFGRS (The 2dF Galaxy Redshift Survey: spectra and redshifts), and the Sloan Digital Sky Survey, or SDSS (The Sloan Digital Sky Survey: Technical summary)(e.g. Springle et al. 2006).

However, even though these observations can show the shape of the Universe at different times, they are not able to explain the process that transformed the very old small density perturbations in the structures seen today, this is the formation of large-scale structures. New tools were required in order to solve those problems, and the answer came with the computer technology. With this new tool, scientist could develop computer simulations that calculated the processes between the well known linear regime to the non-linear regime, being able to connect the early Universe with the current observations.

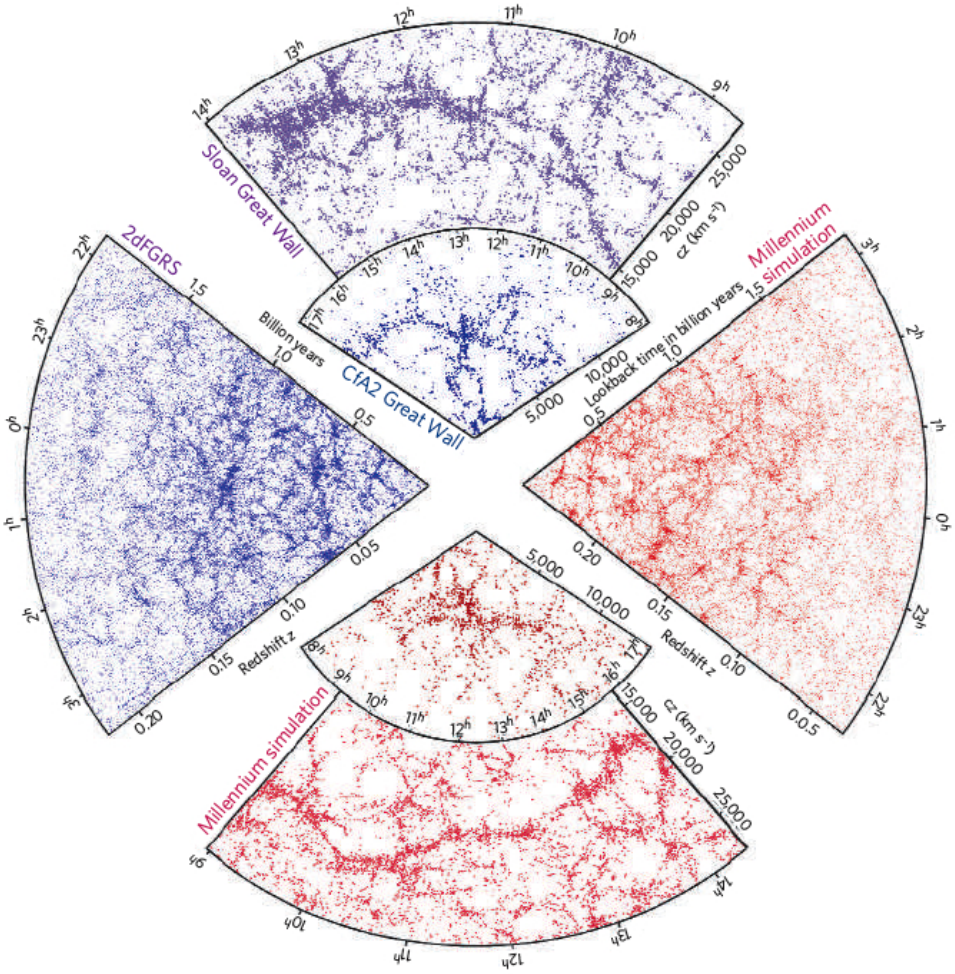

Figure 1.1.1: Galaxy distribution obtained from surveys vs simulations. The blue plots represent the surveys observations, being the left part the 2dFGRS and the top the SDSS. Red plots present the results obtained by the Milennium simulation (Springel et al. 2006)

Using the data from surveys and results given by simulations, a standard model for the Universe has been stated, which says that the Universe is composed mostly by dark energy (73%), dark matter (23%) and baryonic matter (4%), while the Hubble constant has been determined to be 71 ± 2.5 km/s/Mpc (Jarosik et al. 2010). Nevertheless, as history has taught us, these results may not be definitive since new studies and simulations can provide data that disagrees with this model, resulting in the need of newer theories or modifications.

1.2 Aim of the Thesis

The aim of this thesis is to understand the effect of the cosmological parameters in ΛCDM universe and in particular to study the implications due to the presence of hot dark matter. The method used to achieve this goal is performing a variety of simulations using a N-body code in order to test the different cosmologies, modifying the values of a certain range of cosmological parameters e.g. Hubble constant and density parameters, in order to study the results obtained. Using this data it will be possible to understand the effects of these parameters in the formation of large-scale structures in the Universe, the relation between each other and their nature. Especially the cases comparing cosmologies using hot dark matter with others without this component will be tested.

The rest of the thesis is organized as follows. In Chap. 2, some observational background is provided, while in Chap. 3 the theory behind the structure formation and the models that describe the evolution of the Universe are explained. Chap. 4 contains information about simulation codes, as well as the presentation of the code used in this thesis. In Chap.5, the analysis tools used to study the results are introduced. In Chap. 6, the simulations and the results obtained from them are analyzed. In Chap. 7, we draw the conclusions. Finally the Appendix is divided in two parts: firstly simulations of dark halos run to complement the studies done previously, and secondly a list of equations located in the simulation code that have been used to do some theoretical calculations, showing where they can be found.

Chapter 2

Observations

Before explaining the cosmological theory used in the thesis it is very important to have a review of the observations and discoveries achieved during the last years, giving a picture of what has been discovered since the modern cosmology started and how this process has evolved. Obviously, the whole history of cosmology cannot be explained, hence the efforts will be focused on the observations and surveys that have contributed to explain the formation of large-scale structures, as well as the main actors implied in this process, such as dark matter or the Cosmic Microwave Background Radiation.

Moreover, the cosmological parameters studied in the thesis will be presented, describing their meaning, origin and use in the simulations. Needless to say the aim of this chapter is to introduce them, while their influence and effects on the formation of structures is analyzed in more detail in Chap. 6.

2.1 Cosmological Principle

In the beginning of modern cosmology at the first part of the 20th century, there was not too much experimental or observational data that could be used to compare with the theories, therefore some assumptions were needed to develop them, especially assumptions related to some kind of symmetry in the field studied, making possible to erase some degrees of freedom in the system.

Thus, the *Cosmological Principle*, introduced by Eisntein and adopted by the other cosmologist, says that at sufficient large scales the Universe is isotropic and homogeneous. Isotropy is the property of looking the same in all directions, while homogeneity is being identical in any location of the space (Coles & Lucchin 2002). Many observations and surveys have shown that the Universe have these properties, even though they are not completely fulfilled. One example is the study of the Cosmic Microwave Background Radiation [see Sect. 2.2], which reveals that there is some degree of anisotropy in the density distribution of the Universe, even if it is very small. Besides, in order to accept that the Universe is homogeneous from the isotropy observed, the *Copernican Principle* has to be assumed. The Copernican Principle states that humans are not privileged observers, hence the Earth is not a special point in the space with some kind of spherical symmetry around it (Peacock 1999). Therefore when isotropy is accepted together with the Copernican Principle implies homogeneity, resulting in the validation of the Cosmological Principle.

2.2 Cosmic Microwave Background Radiation

At the very firsts moments, the Universe was an infinitesimal volume, having an enormous energy density distributed homogeneously and isotropically. Few moments later, at approximately 10^{-37}s, the Universe started to expand exponentially, in a process known as *cosmic inflation* (e.g. Roos 2008). When inflation stopped, elementary particles were relativistic i.e. they travelled at speed close to the speed of light. After that, the Universe continued to expand and cold down, allowing the formation of baryons ($t = 10^{-6}$s) e.g. protons and neutrons. Is before this period when some neutrinos could decouple still having relativistic velocities and form what is called hot dark matter [see section Sect. 2.3.2].

As the expansion continued the Universe kept on cooling down, and when few minutes had passed since the initial expansion the first nuclei of deuterium, hydrogen and helium formed, in a process called *nucleosynthesis* (e.g. Jedamzik & Pospelov 2009). Around 400,000 years later, when the temperature of the Universe was lower than the ionization temperature, the atoms nuclei and the free electrons could combine into atoms. Thus, radiation could decouple from matter and travel through the space, creating the relic radiation that can be detected now, the *Cosmic Microwave Background Radiation*. Finally, after a long period, stars, galaxies and the others structures started to form, but the exact process is still unknown. Some theories describe a top-down process, where the largest structures are formed firstly and through fragmentation the smaller structures e.g. galaxies and stars are created. On the other side, there is also the possibility that a bottom-up process took place, creating first the stellar-size objects and by hierarchical clustering larger structures such as galaxies and clusters are formed (Yoshida 2009). This second theory of large-scale formation is the one mostly accepted today due to the agreement of the existence of cold dark matter [Sect. 2.3.1].

The Cosmic Microwave Background Radiation (CMBR) was discovered by Arno Penzias and Robert Wilson in 1964, when they detected a radiation in the microwave range of frequency that was coming from all directions in the sky. Even thought the Big Bang model describes an homogeneous and isotropical density dstribution in the early Universe, observations of the CMBR have shown that there is some degree of anisotropies in the temperature profile of the CMBR. Thanks to precise observations done in recent years, it has been determined that the CMBR has a black body spectrum with a temperature of 2.725 K, being the anisotropies small fluctuations in the temperature distribution due to small variations in the density profile of the early Universe.

Since the CMBR was detected, many surveys have been done in order to discover its characteristics. Regarding these surveys, it is interesting to present two of them, the observations done by the COBE and the WMAP satellites, especially the WMAP, which is the tool used in the last years to do the measurements and is offering very precise data of the relic radiation. Thus, the COBE (Cosmic Background Explorer) was a satellite developed by the NASA and launched in 1989, used to confirm many of the predictions done by the Big Bang model. Furthermore, it confirmed that the CMBR had a black body radiation, and showed that its temperature was 2.73 K. It also detected the anisotropies in the CMBR and discovered some early galaxies (Bennett et al. 1993).

On the other side, the WMAP (Wilkinson Microwave Anisotropy Probe) was developed by the NASA as well, and was launched in 2001. The WMAP is used nowadays to study

the CMBR, due to its high precision instruments, which allow the observation of the sky with much more accuracy than before. The WMAP has been used to obtain a large amount of results that have given a more detailed picture of how is the Universe, its formation and its characteristics. Thus, with the observation done by WMAP, it has been determined that the Hubble constant is 71 ± 2.5 km/s/Mpc, the age of the Universe is 13.75 ± 0.13 Gyr, and the fact that the Universe is formed by 73% of dark energy, 4% of ordinary matter and 23% of dark matter (Jarosik et al. 2010).

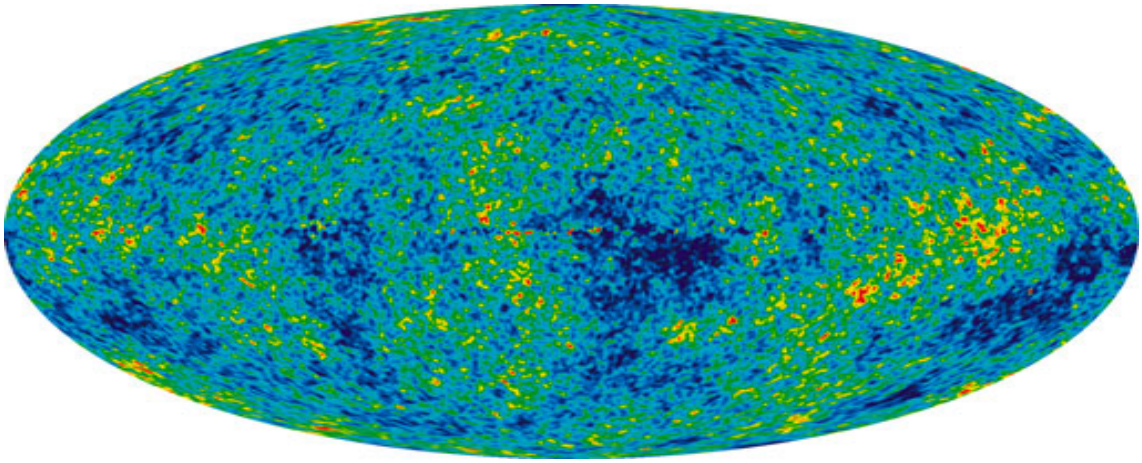

Figure 2.2.1: Map of the CMBR obtained from WMAP. The plot is done using a linear scale from -200 to 200 μK (`http://map.gsfc.nasa.gov/media/101080/index.html`)

2.3 Dark Matter

As it has been said in the previous section, there are two types of matter in the Universe, the ordinary or baryonic matter and the dark matter. The difference between ordinary and dark matter is that dark matter does not emit, absorb or scatter radiation (e.g. Ostriker & Steinhardt 2003). There are two main candidates for dark matter, *hot dark matter* and *cold dark matter*, but throughout the years other elements and ideas have been studied as well e.g. *warm dark matter*. Astronomers think that dark matter content in the Universe is much larger than ordinary matter, representing the atomic matter less than 5% of the mass content in the Universe (e.g. Bennett 2006; Jarosik 2010).

The first one to propose the existence of Dark Matter was Fritz Zwicky in 1933, who observed that the speed of galaxies in large clusters were too large for being explained by the visible matter. Since then, other studies about galactic rotation curves, structure of galaxy groups and clusters, and large scale cosmic flows have pointed out the existence of dark matter as well (e.g. Springel et al. 2006). One of those mismatch is the rotation velocity of spiral galaxies, where gas and stars rotate around the galaxy center in nearly circular orbits, hence these motions should obey Kepler's law [Eq. 2.3.1]. However, observations revealed that their velocities were larger than the expected, suggesting the presence of more matter than the visible one.

$$v = \sqrt{\frac{GM}{r}} \tag{2.3.1}$$

Furthermore, big fluctuations in the density of the Universe are needed to form the structures seen today. Nevertheless, the CMBR do not show fluctuations that important, hence it is not possible for ordinary matter to cause them, since this matter would had printed a signal in the CMBR much bigger than the one that can be observed. An accepted explanation for this, is that this dark matter was the main contributor to the gravity fields, enhancing the gravitational force without leaving any trace in the CMBR.

After this introduction to dark matter, it is possible to present the two main candidates for this type of matter, the cold dark matter and the hot dark matter.

2.3.1 Cold Dark Matter

Cold dark matter (CDM) is composed by particles that decoupled when they were not relativistic, hence their velocities were much less than the speed of light. Thus, their free streaming is of no cosmological importance (e.g. Primack & Gross 2000), resulting in their impossibility of diffusing small fluctuations in the early Universe. For this reason perturbations in small scales would survive and could be the seeds for structures formation.

The true nature of cold dark matter is discussed, because since dark matter does not emit or absorb radiation it is almost impossible to analyze with the present technology. However, some possible candidates for this type of matter have been suggested, being two of them the *Weakly Interacting Massive Particles* (WIMPs) and the *Axions* (e.g. Ostriker & Steinhardt 2003; Agertz 2004).

Since the small fluctuations in density are not dumped out with the CDM, the formation of structures is described as a bottom-up process, where small structures form first and larger structures are created by the merge and addition of smaller structures through what is called hierarchical clustering (Press & Schechter 1974). The hierarchical clustering explains that separate particles collide and remain together forming larger units, and the process is repeated several times creating big structures e.g. planets and galaxies. Hence a picture using cold dark matter predicts that halos of dark matter form around the gaussian fluctuations in density, and then, due to its gravitational potential baryonic matter is attracted. When the baryonic material has been attracted, galaxies form at the centres of these dark halos by the cooling and condensation of gas that fragments into stars. Groups and clusters of galaxies form as halos aggregate into larger systems (e.g. Springel, et al. 2006).

During many years cold dark matter has been the most plausible explanation for dark matter. Nowadays it is still the accepted option, even though scientist have realized that a model using only cold dark matter do not work properly. When comparing simulations with observations it is seen that they do not fit too well. One of the problems arising is the missing of satellite galaxies. These models predicts that a lot of small satellite galaxies would form around the galaxies like our Milky Way, but they are not observed. For these reasons new models have been developed recently to be able to solve these problems e.g. Λ Cold Dark Matter model or the Hot+Cold Dark Matter model.

2.3.2 Hot Dark Matter

Hot dark matter (HDM) is supposed to be formed by light neutrinos with velocities close to the speed of light, which were decoupled sometime after inflation, when particles were still relativistic. The exact mass of these neutrinos is unknown, but in order to satisfy different conditions regarding the Universe density and other considerations their masses are expected to be about ∼eV (e.g. Primack 2001).

Using the Hot Dark Matter model, the first structures to form are the ones with densities of the order of superclusters size, with masses $\sim 10^{15} M_{\odot}$, due to the main property of HDM, the *free-streaming* of light neutrinos. Thus, one year after Big Bang, the temperature of the Universe was about 100 million degrees, which means that particles had a thermal energy of $10^4 eV$, much larger than the rest mass of light neutrinos. These neutrinos would spread out, leading to the smooth and destruction of any fluctuation in densities smaller than superclusters. Using this scenario, the formation of the smaller structures such as galaxies is described by a top-down process, where the first objects to appear are the ones of the size of superclusters, with galaxies and clusters forming after their initial collapse by fragmentation (e.g. Primack & Gross 2000).

At the end of the 70's and the beginning of the 80's HDM seemed to be the answer for the dark matter problem. Numerical simulations showed that regions of high density formed filaments, with the highest densities in the intersections and void between them; a picture that had great similarity with the observations. However, in the mid-80's it was realized that if galaxies formed sufficiently early to fit observations, they would had a much more inhomogeneous distribution than what it could be seen. In addition, studies and simulations showed that any structure would form later than what it can be deduced from observations (e.g. Primack & Gross 2000).

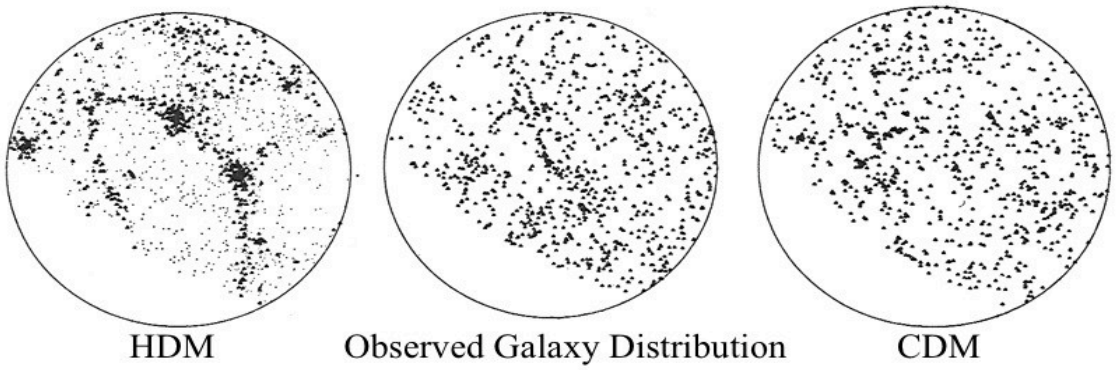

Figure 2.3.1: HDM and CDM simullations compared with the observed galaxy distribution (White 1986)

2.4 Dark Energy

As said in Sect. 2.2, the most part of the Universe is in form of what is called *dark energy*. In order to explain this element, first it is necessary to introduce Eq. (2.4.1), which is the acceleration equation coming from General Relativity when the Cosmological Principle is

considered. In this expression $a(t)$ is the dimensionless scale factor as a function of time, $\ddot{a}$ is its second time derivative, G is Newton's gravitational constant, ρc is the energy density, and p is the pressure.

$$\frac{\ddot{a}}{a} = -\frac{4\pi G}{3c^2}(\rho c^2 + 3p) \tag{2.4.1}$$

From the previous equation when a negative pressure dominates, it is expected to have expansion e.g. the inflation process predicted in the Big Bang Theory. On the other side, if the energy was dominated by the gravity generated by the baryonic and dark matter the expansion of the Universe should decelerate. However, observations of exploding white dwarf stars, the Supernova type Ia, have shown that the Universe is not only expanding, but accelerating. Thus, it seems that there is a contribution in the form of some kind of negative pressure that is added in Eq. (2.4.1), the called dark energy (e.g. Bennett 2006).

Dark energy is a very hot topic in modern cosmology, due to the fact that its presence was not widely accepted until recent times. Since surveys have given evidences of the faster expansion of the Universe, dark energy has been accepted, and nowadays simulations and observations seem to agree with that concept. Nevertheless, the nature of dark energy is even more unknown than dark matter, leading to discussions about its origin and behavior, hence it is a very active field of study.

2.5 Cosmological Parameters

2.5.1 Density Parameters

The *density parameters* represent the amount of a component in the Universe compared with the critical density [Eq. (2.5.1)], therefore they tell how much a component of the Universe contributes to the density comparing with the case of a flat Universe. To be precise, the density parameters studied in this thesis are the *matter density*, being its contributors dark matter and baryonic matter, and the Λ *density* [see Eq. (2.5.2)]. Nevertheless, if these concepts are not familiar, further explanation can be found in Chap. 3.

$$\rho_c = \frac{3H^2}{8\pi G}, \tag{2.5.1}$$

$$\Omega_m \equiv \left(\frac{8\pi G}{3H_0^2}\right)\rho_0 \qquad \Omega_\Lambda \equiv \frac{\Lambda}{3H_0^2} \tag{2.5.2}$$

Thus, since a flat Universe is considered, the summation of both densities must be equal 1

$$\Omega_m + \Omega_\Lambda = 1 \tag{2.5.3}$$

meaning that the total density of the Universe is equal to the critical density [see Eq. (2.5.1)]. This condition implies that only one of the densities can be freely modified, since the other value will be restricted by Eq. (2.5.3).

Changing the value of these densities affects the composition of the Universe, and consequently, the structure formation occurred in it. Thus, large matter density will mean that most of the Universe is in form of matter, baryonic and dark, resulting into the fact that the gravity is the main actor in the play; while large values of dark energy density will lead to a Universe where the gravity forces have less effect compared to the motion due to Lambda.

2.5.2 Amplitude of Galaxy Fluctuations: σ_8

The mass variance is a tool that describes how the mass is distributed depending on the scale considered. Usually, a specific value of this mass variance is used in the simulations in order to define the initial state of the system studied, allowing to set the initial conditions for a simulated universe. This especial value is known as σ_8 or *Amplitude of galaxy Fluctuations*, and it is defined as the linearly evolved root-mean-squared of the mass fluctuations in a sphere with radius of $8h^{-1}Mpc$ at the present time (e.g. Jing et al. 1995)

$$\sigma_8^2(8h^{-1}Mpc) = \frac{1}{2\pi^2}\int_0^\infty P_{lin}(k)W^2(kr)k^2\,dk \tag{2.5.4}$$

where $W(x)$ is the top-hat function and P_{lin} is the *Linear Power Spectrum* [see Sect. 5.2]

$$W(x) = \frac{3}{x^3}(\sin x - x\cos x). \tag{2.5.5}$$

This value gives information about the current state of the Universe if the system had evolved in the linear regime, hence, it can be used to extrapolate information about the amplitude of the initial density fluctuations of the Universe, helping to find the initial conditions of the universe studied.

2.5.3 Scalar Spectral Index

As it will be seen in Sect. 3.2.1, the initial power spectrum calculated theoretically is proportional to k^n. The n exponent is known as the *Primordial Tilt* or *Scalar Spectral Index*, and changing its value varies the shape of the initial power spectrum. Thus, increasing the tilt leads to larger power at smaller scales than in the case with low n, and decreasing it means that smaller scales have less power. Therefore the power, hence the amplitude of the density perturbations, will be changing depending on the scales when this tilt is modified.

2.5.4 Hubble Constant

In cosmology h and H_0 represent the *dimensionless Hubble parameter* and the *current Hubble parameter* i .e. the *Hubble constant* $H_0 = h\cdot 100\,\mathrm{kms}^{-1}\mathrm{Mpc}^{-1}$. The Hubble cosntant is fundamental because it describes how the objects are separating in relation to each other, in other words, it determines the expansion rate of the Universe. However, the Hubble parameter is not constant, it changes with time, thus the Hubble parameter for a certain time t varies [see Eq. (3.1.8)], and it depends on a, the expansion factor.

Hence a large h means faster expansion of the Universe, since the expansion factor increase is larger. This does not affect the shape of the Universe and the structures formed, but it modifies the velocity of this structure formation. Thus, large values of h will lead to faster expansion and consequently to an earlier structure formation.

Mathematically the Hubble constant interacts with the expansion rate of the Universe through the *growth factor* [see Eq. (3.2.15)] (Padmanabhan 2002). The growth factor shows how the Hubble parameter, and hence the expansion parameter a, determine the growth of the density perturbations in the Universe. Nevertheless, Eq. (3.2.15) can only be used

in the linear regime since the equation is derived using linear and Newtonian theory and does not take into account the non-linear effects that appear in the system at later times.

2.5.5 Quadrupole Moment

Taking into account the Cosmological Principle, the Universe is supposed to be homogeneous and isotropic. Thus, the Cosmic Microwave Background Radiation should be isotropic as well, since it presents the remains of the ancient radiation generated at very early times. However, some studies, many of them using data from the WMAP satellite, have shown that there are some degrees of anisotropies in this radiation. It is possible to find two main contributors to this anisotropy, the called dipole and quadrupole moment. These anisotropies are given by

$$\frac{\Delta T_d}{T_0} = \frac{T(\theta) - T_0}{T_0} \frac{1}{\cos(\theta)} \tag{2.5.6}$$

where $\Delta T_d/T_0$ is the anisotropy, T_0 is the mean temperature, and $T(\theta)$ the temperature for a certain angular position in the sky (Coles & Lucchin 2002). Depending on the value of θ the dipole or the quadrupole moment can be calculated.

On one hand, the dipole anisotropy is expected to be caused by the motion of the observer, this means us, and shows the anisotropy for a variation of 180º in the sky. On the other hand, the quadrupole moment is defined as the level of anisotropy in the Cosmic Microwave Background Radiation, but this time for a variation of 90º in the sky. Thus, the anisotropy of the CMB can be estimate approximately without taking into account the motions of the observer. The quadrupole moment has been determined using the COBE and the WMAP satellites with a certain range of uncertainty, having in the last version of WMAP results a value of $197^{+2972}_{-155}\mu$ K^2 (Jarosik et al. 2010). In order to avoid any misunderstanding when using this parameter, it is very important to point out that the values presented in the WMAP reports are the square of the quadrupole moment, as it can be observed in the units they have. Thus, the real quadrupole value will be the square-root of the value appeared in the WMAP results.

Chapter 3

Theory

It is not the aim of this thesis to give a detailed explanation of the General Relativity Theory, hence the very long maths behind all this theory and some of the concepts and the processes needed to solve it will be avoid. Thus, it will be possible to focus in the meaning of the equations obtained from the theory, the terms that form them and the use of each one. However, this does not mean that all this mathematical background is not important, since is the base that supports all this science, but it would take a very long time to try to introduce all the theory. For that reason if it is the interest of the reader to know all the concepts and solutions to the relativity equations and the different metrics used, very detailed explanations can be found in many books (e.g. Peacock 1999; Padmanabhan 2002; Coles & Lucchin 2002).

3.1 Friedmann Model

After this short introduction, it is time to give a general review about the models and theories behind the study of large-scale structures formation and behaviour.

When the Universe is observed it can be seen that there are many inhomogeneities in the matter distribution e.g. stars, galaxies and clusters of galaxies. But if the Universe is studied at sufficient large scales the Cosmological Principle can be accepted, leading to a homogeneous and isotropic 3D-space. From this starting point, let us consider a particle or a region with mass m and radius r, and equal the kinetic and the gravitational potential energy ($v^2/2$ and $-GM(r)/r$)

$$\frac{1}{2}\dot{a}^2 - \frac{4\pi G\rho(t)}{3}a^2 = constant, \tag{3.1.1}$$

resulting in

$$\frac{\dot{a}^2}{a^2} + \frac{k}{a^2} = \frac{8\pi G}{3}\rho(t). \tag{3.1.2}$$

This is known as *Friedmann equation*, and *a(t)* represents the *expansion factor*, which relates the proper and the commoving coordinates $r = ax(t)$, defined as

$$1 + z(t) \equiv \frac{a(t_0)}{a(t)}. \tag{3.1.3}$$

From Einstein's equations a second independent equation can be found

$$\frac{2\ddot{a}}{a}\frac{\dot{a}^2}{a^2} + \frac{k}{a^2} = -8\pi G p, \tag{3.1.4}$$

being $p = p(\rho)$ the equation of state. Combining Eqs (3.1.2) and (3.1.4) it is obtained:

$$\frac{k}{a^2} = \frac{8\pi G}{3}\rho - \frac{\dot{a}^2}{a^2} = \frac{\dot{a}^2}{a^2}\left[\frac{\rho}{(3H^2/8\pi G)} - 1\right]. \tag{3.1.5}$$

In the previous equation appears for the first time a very important parameter, the *critical density*,

$$\rho_c = \frac{3H^2}{8\pi G}, \tag{3.1.6}$$

which allows to define the density parameters [Eq. (3.1.7)], being them the proportion of the density of one component of the Universe regarding the critical density. Thus, the *matter density* Ω_m, the *dark energy density* Ω_Λ and the *curvature density* Ω_k are introduced.

$$\Omega_i = \frac{\rho_i}{\rho_c}. \tag{3.1.7}$$

Most of the researches and surveys point out that we live in a flat Universe without any curvature, $\Omega_k = 0$, where the total density of the Universe is equal to the critical density. Moreover, usual values accepted for the matter and dark energy densities are $\Omega_m \approx 0,27$ and $\Omega_\Lambda \approx 0,73$ respectively (Jarosik et al. 2010). In the case the Universe was not flat, two possibilities have to be taken into account. On one side, it could be a closed Universe where the density is larger than the critical density $\Omega > 1$; and on the other side, an opened Universe scenario appears with $\Omega < 1$.

Another important element in Eq. (3.1.5) is the *Hubble parameter*

$$H(t) = \frac{\dot{a}}{a}, \qquad h = \frac{H_0}{100km\ s^{-1}Mpc^{-1}}, \tag{3.1.8}$$

that defines the expansion rate of the Universe. Finally, using this new definitions, Eq. (3.1.2) becomes

$$H^2 = \frac{\dot{a}^2}{a^2} = H_0^2\left[\Omega_r(1+z)^4 + \Omega_m(1+z)^3 + \Omega_k(1+z)^2 + \Omega_\Lambda\right], \tag{3.1.9}$$

where it possible to define the *Hubble radius*

$$d_H(z) = H_0^{-1}\left[\Omega_r(1+z)^4 + \Omega_m(1+z)^3 + \Omega_k(1+z)^2 + \Omega_\Lambda\right]^{-1/2}. \tag{3.1.10}$$

With this a basic knowledge of the Friedmann model and the concepts involved in it has been presented. Nevertheless, even if the ideas and procedures needed to obtain them have been introduced here, the cosmological and mathematical background necessary to obtain and understand them is much deeper. For that reason, if it is considered adequate, a more detailed explanation of all the derivations and theory behind these concepts can be found in Peacock Chap. 3 (1999) and Padmanabhan Chap. 3 (2002).

3.2 Linear Regime

When a perturbation mode enters the Hubble radius, then the density perturbation can be treated using Newtonian theory, which leads to the linear regime study. In this situation the density perturbations have the form of a density background value ρ_0, which is constant for all the space, and a small density contribution $\delta\rho$ coming from the inhomogeneity of the density field. The main condition in order to apply the linear regime theory is that the adimensional density fluctuations must be much less than unity. Eq. (3.2.2) presents the adimensional density fluctuations, where $\rho(\mathbf{x})$ is the density value for a certain position and $\bar{\rho}$ is the density background.

$$\rho = \rho_0 + \delta\rho \tag{3.2.1}$$

$$\delta(\mathbf{x}) = \frac{\rho(\mathbf{x}) - \bar{\rho}}{\bar{\rho}}. \tag{3.2.2}$$

Another approach to know if the fluctuations can be treated by the linear regime is to study the mass variance. Since the mass variance is normalised using different functions and tells information about the diversity of the fluctuations, it can be studied in the same manner than the density fluctuations. Thus, values of σ^2 much less than unity point out that the linear regime governs these modes, while mass variances larger than one mean that the fluctuations are not inside the linear regime.

$$|\delta| \ll 1 \rightarrow \sigma^2 < 1 \tag{3.2.3}$$

$$|\delta| \geq 1 \rightarrow \sigma^2 > 1. \tag{3.2.4}$$

Once it is proved that the system evolves in the linear regime, commoving coordinates can be chosen for particles positions and velocities expressing the position coordinate as $\mathbf{r}(t) = a(t)\mathbf{x}(t)$, which satisfies the condition

$$\ddot{\mathbf{r}} = -\nabla_{\mathbf{r}}\Phi, \tag{3.2.5}$$

being Φ the gravitational potential. Similarly as it has been done with the density, the gravitational potential can be presented as a combination of a background and a perturbation component

$$\Phi = \Phi_b + \phi, \tag{3.2.6}$$

and then expanding the position coordinate and operating with Eq. (3.2.5) it can be found

$$\ddot{\mathbf{x}}_i + \frac{2\dot{a}}{a}\dot{\mathbf{x}}_i = -\frac{1}{a^2}\nabla_{\mathbf{x}}\phi \qquad \nabla_x^2\phi = 4\pi G a^2 \rho_b \delta. \tag{3.2.7}$$

Now that the particle trajectories are related to the background density, it is interesting to write a differential equation for $\delta(t, \mathbf{x})$, or what it will be easier, $\delta_{\mathbf{k}}(t)$, which is the adimensional density fluctuations in the k-space. Thus, the first step is to define $\rho(\mathbf{x}, t)$ thinking that the density is caused by the summation of the points in that coordinate, each one with mass m:

$$\rho(\mathbf{x}, t) = \frac{m}{a^3(t)} \sum_i \delta_D \left[\mathbf{x} - \mathbf{x}_i(t)\right]. \tag{3.2.8}$$

The density contrast $\delta(\mathbf{x},t)$ is then related to the density $\rho(\mathbf{x},t)$ through

$$1+\delta_D(\mathbf{x},t) \equiv \frac{\rho(\mathbf{x},t)}{\rho_b} = \frac{V}{N}\sum_i \delta_D\left[\mathbf{x}-\mathbf{x}_i(t)\right] = \int d\mathbf{q}\delta_D\left[\mathbf{x}-\mathbf{x}_T(t,\mathbf{q})\right], \tag{3.2.9}$$

where N is the total number of particles inside the volume V, and $\mathbf{q}$ represents a set of physical quantities that define a certain particle T. With this is possible to calculate the Fourier transform of the density contrast

$$\delta_{\mathbf{k}}(t) \equiv \int d^3\mathbf{x}e^{i\mathbf{kx}}\delta(\mathbf{x},t) = \int d\mathbf{q}\ \exp[-i\mathbf{k}\,\mathbf{x}_T(t,\mathbf{q})] - (2\pi)^3\delta_D(\mathbf{k}), \tag{3.2.10}$$

and differentiating and using Eq. (3.2.7) the *perturbation equation* is obtained:

$$\ddot{\delta}_{\mathbf{k}} + 2\frac{\dot{a}}{a}\dot{\delta}_{\mathbf{k}} = 4\pi G\rho_0\delta_{\mathbf{x}} + A_{\mathbf{k}} - B_{\mathbf{k}}, \tag{3.2.11}$$

where $A_{\mathbf{k}}$ and $B_{\mathbf{k}}$ can be ignored since the linear regime is considered, resulting in:

$$\ddot{\delta}_{\mathbf{k}} + 2\frac{\dot{a}}{a}\dot{\delta}_{\mathbf{k}} = 4\pi G\rho_0\delta_{\mathbf{x}}. \tag{3.2.12}$$

Once the perturbation equation has been determined, it is of great interest to study how the perturbations evolve in the Universe. Nevertheless, this is very difficult to do because the solution to these equations needs of numerical methods to be done, hence it is a good alternative to make some simplifications in order to get analytical results. First we can assume that $\rho(t)$ is a solution of the Friedmann equations, and also introduce the function $\rho_1 \equiv \rho(t+\epsilon)$, beign ϵ a certain constant. With this, the density contrast can be written as

$$\delta(t) = \frac{\rho_1(t)-\rho(t)}{\rho(t)} = \frac{\rho(t+\epsilon)-\rho(t)}{\rho(t)} \cong \epsilon\frac{d\ \ln\rho}{dt} = -3\epsilon H(t), \tag{3.2.13}$$

showing that $H(t) \equiv (\dot{a}/a)$ is a solution to the perturbation equation. It is known that $H(t)$ is a decreasing function with mode δ_d; however, the interesting point is the increasing mode δ_g, which is given by

$$\delta_g = \delta_d\int\frac{dt}{a^2\delta_d^2} = H(t)\int\frac{dt}{a^2H^2(t)} = H(a)\int\frac{da}{(Ha^3)}. \tag{3.2.14}$$

The increasing mode, or *growth factor*, can also be written as

$$\delta_g(a) = \frac{5\Omega_m}{2}H(a)\int_0^a\frac{dx}{\left(xH(x)\right)^3}, \tag{3.2.15}$$

where δ_g is normalised with $a=1$ and $H=1$ at the present epoch, and $H(a)$ is defined as follows (see Padma Eq. (5.121)):

$$H(x) = \left[\Omega_m x^{-3} + \Omega_\Lambda + (1-\Omega_m-\Omega_\Lambda)x^{-2}\right]^{1/2}. \tag{3.2.16}$$

Fig. 3.2.1 shows how the growth factor varies with time and also with the mean densities of matter and dark energy. This occurs because the current Hubble constant is dependant

on the different mean densities [Eq. (3.2.16)]. It can be observed that the growth factor increases as it approaches the present time, but the proportion of dark matter and dark energy modifies it. Thus, at high redshifts (small values of a) the amount of dark matter and dark energy does not affect very much, but as the time increase, different proportions of dark energy and matter lead to different curves. The case with low dark energy density and high proportion of matter density presents higher values of the growth factor, resulting in more developed structures in the Universe than the opposite case, which has a growth factor lower than the previous situation.

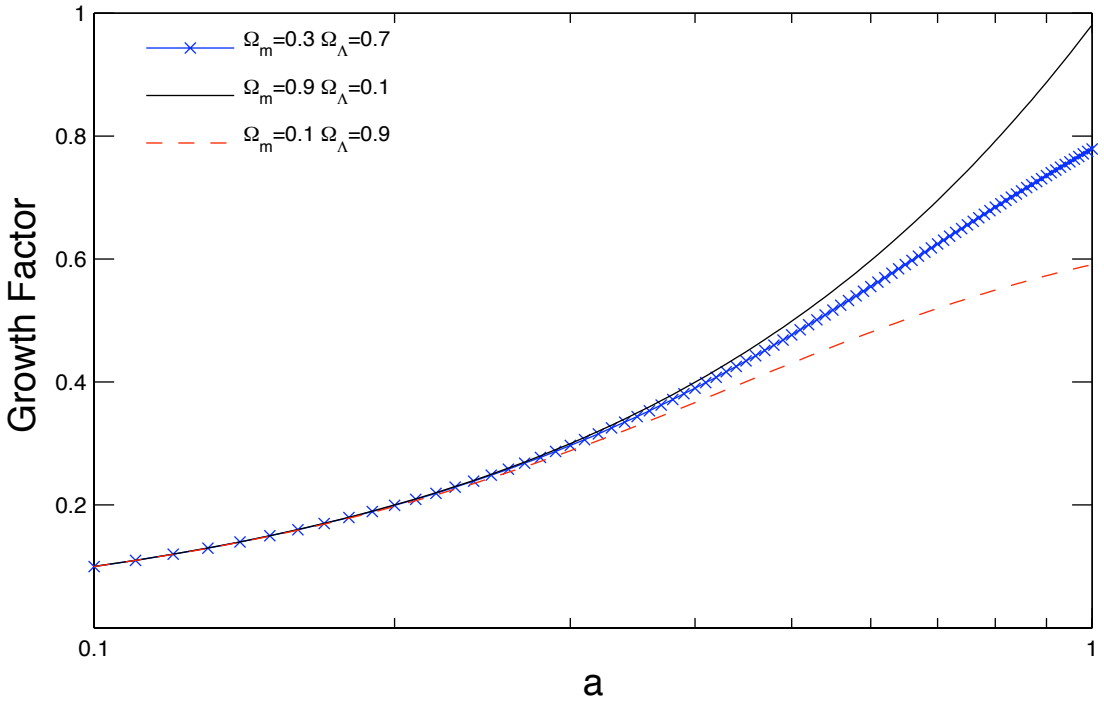

Figure 3.2.1: Evolution of the Growth Factor at different epochs. The dashed red line corresponds to an universe with $\Omega_m = 0.1$ $\Omega_\Lambda = 0.9$, the crossed blue line $\Omega_m = 0.3$ $\Omega_\Lambda = 0.7$ and the solid black line $\Omega_m = 0.9$ $\Omega_\Lambda = 0.1$

Eq. (3.2.15) can be solved numerically using different methods, but it is also possible to obtain an analytical approximation using elliptical functions (for a more detailed resolution see Sect. 2.5.2 in Agertz (2004)). Considering the case of $\Omega_m = 0.3$ and $\Omega_\Lambda = 0.7$, Eq. (3.2.15) can be expressed as Eq. (3.2.17), where it can be seen that for small values of a the growth factor is almost proportional to the expansion parameter, hence the density perturbations grow in proportion to that.

$$\delta_g(a) = a - \frac{2}{11}\frac{\Omega_\Lambda}{\Omega_m}a^4 + \bigcirc(a^7) \tag{3.2.17}$$

Further explanations and more information about the concepts and procedures presented in this section are available in Peacock Sect. 15.2 (1999) and Padmanabhan Sects 5.5 and 5.6 (2002).

3.2.1 Linear Power Spectrum

Now the linear regime is explained, it is time to introduce a very important concept when studying the statistical properties of the Universe, the *Linear Power Spectrum*. The power spectrum studies the distribution of power when considering the different perturbation modes present in the system $\delta(\mathbf{x}, t)$, which are characterized by their initial state $\delta(\mathbf{x}, t_i)$. Firstly, let us assume that each density perturbation mode $\delta(\mathbf{x}, t)$ has a Fourier transform $\delta_{\mathbf{k}}(t_i)$. Thus, for a very small t_i, each Fourier mode can be considered as a Gaussian random variable with

$$\langle \delta_{\mathbf{k}}(t_i)\delta_p^*(t_i)\rangle = (2\pi)^3 P(\mathbf{k}, t_i)\delta_D(\mathbf{k}-\mathbf{p}), \tag{3.2.18}$$

being $P(\mathbf{k}, t_i)$ the *Power Spectrum* of $\delta(\mathbf{x}, t_i)$. This power spectrum for a certain time t can be expressed as

$$P(\mathbf{k}, t) = |T_{\mathbf{k}}(t, t_i)|^2 P(\mathbf{k}, t_i), \tag{3.2.19}$$

where $T_{\mathbf{k}}(t, t_i)$ represents the *Transfer function*, which relates the original power spectrum with the power spectrum of the density perturbation mode for any time. Thus, the power spectrum shows the amplitude, hence the power contained in each one of the perturbation modes, and it reveals information about the power distribution depending on the wavelengths of the density perturbations. Studying the power spectrum it can be seen which modes have more power, presenting the wavelengths where the density perturbations are larger.

The power spectrum can also be calculated with a dimensionless form Δ_k^2, given by

$$\Delta_k^2 \equiv \frac{k^3 P(k)}{2\pi^2}, \tag{3.2.20}$$

where $P(k) = |\delta_k|^2$ is the power spectrum for an isotropic and homogeneous universe. Moreover, it is widely assumed that

$$P(k) = \delta_k^2 \propto k^n, \tag{3.2.21}$$

which leads to the study of the effect of n, also known as the *Scalar Spectral Index* or *Primordial Tilt*. In the ambit of this thesis, only the effects of n in the power spectrum are considered, having a deeper explanation and analysis in Chap. 6. Nevertheless, a rough review can be done in this part, since Eq. (3.2.21) shows that varying the value of n, the slope of the power spectrum will change, resulting in different distribution of the power depending on the scales considered.

More information about this section is available in Padmanabhan Sect. 5.8 (2002).

3.3 Quasi-Linear Regime: the Zeldovich Approximation

After the linear regime, perturbations grow enough to leave that regime and enter the non-linear one, since $\delta > 1$. In this regime, the expressions and theory presented previously do not work, and often N-body methods are used in order to obtain results. However, when using this kind of methods and simulations, the results obtained cannot be reason

out completely. Trying to avoid these problems, some approaches to the non-linear regime have been develop to simplify in some degree the equations involved and get analytical expressions that can describe this simplified model. One of those approaches is the *Zeldovich approximation*, which leads to the study of the *quasi non-linear regime*.

In the Zeldovich approximation, the initial displacement of the particles is found, and then it is assumed that they continue to travel in the same direction. Thus, their trajectories can be written as

$$\mathbf{x}_T(a, \mathbf{q}) = \mathbf{q} + \mathbf{L}(a, \mathbf{q}), \tag{3.3.1}$$

where $\mathbf{q}$ is the original position of the particle and $\mathbf{L}(a,\mathbf{q})$ is the displacement. From the Fourier transform of the density contrast and using the fact that in the linear regime displacements are very small, it can be deduced that trajectories are linear in a (Padmanabhan 2002), resulting in the expression:

$$\mathbf{x}_T(a, \mathbf{q}) = \mathbf{q} + a\mathbf{u}(\mathbf{q}). \tag{3.3.2}$$

Thus, the Zeldovich approximation applies these trajectories to the quasi-linear regime, relating the Eulerian prosition $\mathbf{r}$ of a particle to the Lagragian position $\mathbf{q}$ by

$$\mathbf{r}(t) \equiv a(t)\mathbf{x}(t) = a(t)\left[\mathbf{q} + a(t)\mathbf{u}(\mathbf{q})\right], \tag{3.3.3}$$

being $\mathbf{x}$(t) the commoving Eulerian coordinate. On the other side, the density can be obtained using conservation of mass, given by

$$\rho(\mathbf{r}, t)d^3\mathbf{r} = \hat{\rho}d^3\mathbf{q}. \tag{3.3.4}$$

Finding an expression for $\rho(\mathbf{r}, t)$ and using the Jacobian of its denominator the matrix obtained can be dioganalized, resutilng the final expression

$$\rho(\mathbf{r}, t) = \frac{\rho_b(t)}{\left[1 - a(t)\lambda_1(\mathbf{q})\right]\left[1 - a(t)\lambda_2(\mathbf{q})\right]\left[1 - a(t)\lambda_3(\mathbf{q})\right]}, \tag{3.3.5}$$

where λ_i denotes the eigenvalues defining the principal directions in which the collapses of the structures will occur. Moreover $\mathbf{q}$ can be expressed as a function of $\mathbf{r}$ using Eq. (3.3.3).

Thus, the Zeldovich approximation presents a scenario where the material contained in a certain volume collapse due to gravity. This collapse is firstly produced in one direction defined by one of the eigenvalues of Eq. (3.3.5), compressing the material in a two dimensional sheet shape known as *pancake*. Then the collapse continues in another direction, compressing the material in a filament-like shape and finally another contraction is produced in this last direction. For that reason it can be said that the Zeldovich approximation describes an structure formation divided in many steps, each one characterized by the contraction of material in one direction.

As it has been said in the previous section, additional information and deeper description of these processes can be found in Peacock Sect. 15.8 (1999) and Padmanabhan Sect. 5.9 (2002).

3.4 Non-Linear Regime

Once the linear regime is completely abandoned, and the density perturbations grow more than the linear limit, it is necessary to study the perturbations in the *non-linear regime*. In this regime it is considered $\delta > 1$, and since the linear and quasi-linear equations cannot be used other approaches appear. One of them is the *Sphercial Approximation*, that satisfies

$$\mathbf{x}(t, \mathbf{q}) = f(t)\mathbf{q}, \tag{3.4.1}$$

which means that the particles trajectories are homogeneous, being $f(t)$ a function to determine.

Thus, the spherical model considers a spherical region with a certain overdensity. As the Universe expands, the sphere grows as well; however this expansion is slowed by the overdinsity. After some time, the sphere reaches a maximum radius and then the collapse of the sphere begins. Nevertheless, the collapse will be stopped at some point due to dissipative effects that will transforms kinetic energy due to the collapse into random motion of particles. This last process is the *virialization*, where the equilibrium the sphere will finally reach is given by

$$E_p = -2E_k, \tag{3.4.2}$$

called *virial theorem*, which realtes potential energy E_p with kinetic energy E_k.

Even thought this approximation is useful for having some equations of the system evolution in this regime and it gives a general picture of the structure formation, when large systems want to be studied it is necessary to use numerical methods in order to solve the equations. One of those methods, the one used in this thesis is the N-body simulation, where a numerical program solve the potential gravity field equations reiteratively, simulating the evolution of a system.

Chapter 4

Simulation Codes

The study of large-scale structures in the Universe, how they form and interact between each other is an extremely complicated field that requires the use of very complicated maths. Thus, since computers appeared in the scene, it has become a common approach to use computers to simulate that structure formation. Computers allow the calculation of the non-linear regime equations using numerical methods that otherwise would require extremely long time, making possible to study how the Universe evolves and developes at very large scales. Nevertheless, these simulations have disadvantages, needing computational resources that are not always available and showing errors coming from the numerical approximations. Furthermore, simulations sometimes act as a "black box", leading to a very difficult understanding of the reasons behind the results obtained.

The codes that simulate the Universe can be divided in two main groups: *N-body simulations* and *hydrodynamic codes*. The general characteristics, as well the basic information about how those codes work will be provide, giving a general knowledge to understand the processes and the computations those codes have to do in order to complete the simulations. In addition, the code used in this thesis will be explained in more detail, including the process to generate the initial conditions. The part of the code responsible for finding the dark halos will be also explained, since those files have been utilized to perform some test included in Appendix A.

4.1 N-body Codes

N-body codes represent the system with a discrete number of particles, characterizing those particles with some properties e.g. mass. Thus, the particles interact between them due to those properties and the system evolve. This type of codes are collisionless, therefore these codes are a very good option when large-scales structures formed by dark matter are considered, since this matter is assumed to be collisionless as well.

There are different manners to perform N-body codes, resulting in many types of codes that can be classified as follows: *Particle-Particle* (PP) codes, *Particle-Mesh* (PM) codes, *Particle-Particle/Particle-Mesh* (P^3M) codes, and *Tree* codes.

4.1.1 Particle-Particle (PP)

PP codes place the particles into the simulations box and then calculate the force acting on each particle using summation. Once the force is computed, it is introduced into the equations of motion, obtaining the accelerations and velocities of particles. With these values the particles are moved to their new positions, the time in the simulation is increased and the procedure is repeated again.

One of the biggest problems of these codes is that the force is calculated summing the Newtonian gravity force, which for small interparticle distances can vary largely very rapidly. Thus, PP codes are the easiest ones to implement, since the equations and methods they use are rather simple, but at the same time the least efficient, since they need large amount of computational resources in order to run the simulations.

4.1.2 Particle-Mesh (PM)

The main difference respect to PP codes is that PM codes use a mesh to distribute the mass of the particles, calculating the density and the potentials in the mesh. Hence the code divide the simulation box using a mesh (grid), where the particles are placed and the mass is transfered from the particles to the grid. This can be done by several methods e.g. Nearest Grid Point (NGP) or Cloud In Cell (CIC). Then the Poisson's equation is solved in the grid, and the force field is calculated. After that, the force field is interpolated in order to obtain the force acting on each particle, which is used in the equations of motion to compute the particle displacements. Finally, the time in the simulation is increased and the process starts again.

PM codes have proved to be faster than other methods, and can use a large number of particles to have better resolution. However, the mesh is placed regularly in all the box, hence some locations can have too many grid resolution for the few particles placed there, while in other parts smaller grid distance would be required. Many PM codes are available and have been used regularly in simulations (e.g. Klypin & Holtzman 1997).

4.1.3 Particle-Particle/Particle-Mesh (P^3M)

P^3M codes are a combination of PM and PP codes, where the PM part is used to calculate the large-scale forces, while the PP code solves the small-scale interactions. It could seem that this is the perfect solution for the N-body codes, nevertheless P^3M programs present their own problems. It is common that the code results dominated by the PP part when too many particles are taken into account, leading to the use of more computational resources and needing more time to run the simulations.

Trying to solve the problems those codes showed, some variations have been developed. Thus, adaptive codes (e.g. Couchman 1991) are able to subdivide the grid in a certain zone if too many particles are found, making possible to continue the calculations.

4.1.4 Tree

The main idea in the Tree codes is to compute forces using direct summation when particles are close to each other, while very separated particles are considered as "pseudo-particles".

The denomination for these codes comes from the method used to implement the cells in the simulation box. Firstly, the box is divided into 2^D smaller cells, being D the dimension of the simulation. If a cell contains more than one particle is divided again in more "sub-cells". The process is repeated until each cell has only one particle inside. Thus, at the end of this procedure, the cells present a distribution with a tree shape, where the box is the root, which is divided into twigs and finally into leaves. Once this is done, the properties e.g. mass and center of mass, are calculated for the leaves, the twigs and the root.

As said before, the calculation of the force depends on the distance between particles. The criteria to decide when two particles are considered to be close to each other is defined by a tolerance parameter, which can be modified for decreasing the number of calculations or in the other side, obtaining more precision. Tree codes are available in many sources and have proved their versatility (e.g. Barnes & Hut 1986; Springel et al. 2001).

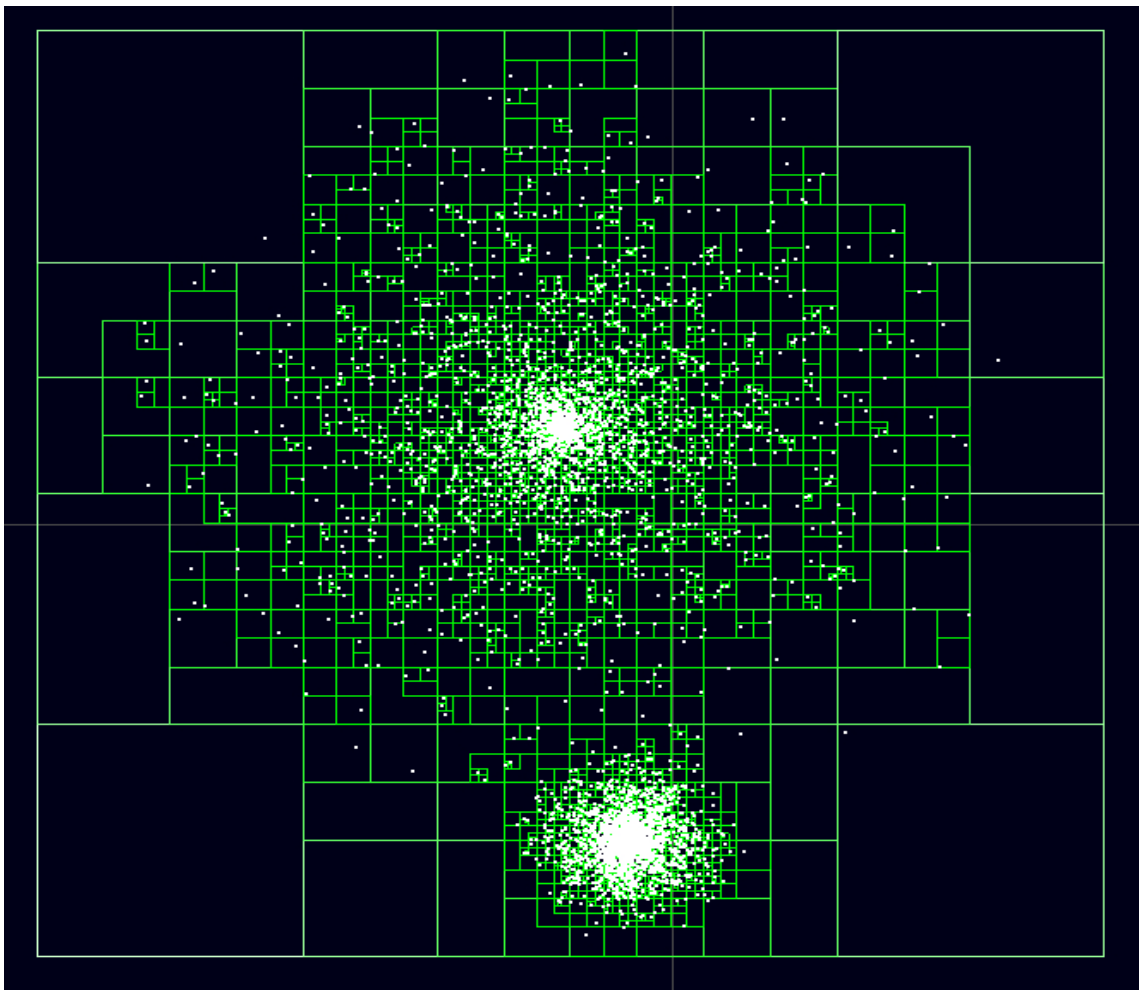

Figure 4.1.1: Simulation using Tree code showing the tree shape for the cell distribution (`http://www.beltoforion.de/barnes_hut/barnes_hut_de.html`)

4.2 Hydrodynamics Codes

In hydrodynamics codes the particles are not collisionless, hence they can interact directly with each other. There are two approaches when treating hydrodynamics codes: the *Smooth Particle Hydrodynamics* (SPH) that follow the Lagrangian motion of gas, and the methods using Eulerian grids to study the gas (Agertz et al. 2007). These type of codes are used to calculate physics that cannot be treated by N-body codes, which not include the fluid consideration of the systems, e.g. hydrodynamics codes have been combined with shock capturing methods in order to be able to calculate density and entropy jumps at shocks (e.g. Ryu et al. 1993).

On one hand, in the SPH the mass elements are followed using classical dynamics but assigning thermodynamic variables e.g pressure, to the particles. Therefore the motion of the particles can be affected by pressure gradients being possible to study hydrodynamic effects such as shocks and some dissipative effects (e.g. Kang et al. 1994). There are different approaches applying the SPH principles due to the fact that many different codes have been adapted: TSPH code uses the Tree method developed by Barned & Hut (1986) and PSPH does the same with the P^3M code (Efstathiou & Eastwood 1981).

On the other hand, codes based upon Eulerian grids simulate the fluid not considering the particles but using a mesh. Thus, Eulerian codes solve the equations using the information contained in the cells, while SPH calculate the properties of the gas considering the closest particles and their interactions. Comparing the two approaches, Lagrangian codes concentrate the resources in the zones with higher interest since they follow the fluid elements, while Eulerian codes have a fixed grid (e.g. Kang et al. 1994). However, in order to solve this problem, adaptive mesh refinement (AMR) codes have appeared recently, which can modify the refinement of the mesh in order to achieve better resolution (e.g. Zhang & MacFadyen 2006).

4.3 The Code Used in This Thesis

In this section the code used for our simulations is going to be presented, showing a picture of its parts and the purpose of each one of its programs. Needless to say the complete presentation and explanation of the code is available in the original article of the code, where all the necessary information to run the programs is explained (see Klypin & Holtzman 1997).

4.3.1 Basic Information

The code used is a Particle-Mesh (PM) code developed by Anatoly Klypin and Jon Holtzman (1997). The advantages of using PM codes is that they are fast, since the number of calculation is lower than other type of codes e.g. TREE codes, and they can use a very large number of particles. This means that they can have rather good resolution of the density and potential calculated, however, it can be a weakness as well, due to the fact that if the number of particles is not large enough the resolution and the results computed will be disturbed.

For solving the equations, the code uses commoving coordinates $\mathbf{x} = \mathbf{x}(t)$ related to proper coordinates by $\mathbf{r} = a(t)\mathbf{x}$. Thus, dimensionless variables are defined as

$$\mathbf{x} = x_0\tilde{\mathbf{x}}, \qquad t = \tilde{t}/H_0, \tag{4.3.1}$$

$$\mathbf{v}_{pec} = (x_0 H_0)\,\tilde{\mathbf{p}}/a, \qquad \phi = \tilde{\phi}\,(x_0 H_0)^2\,, \tag{4.3.2}$$

$$\rho = \frac{\tilde{\rho}}{a^3}\frac{3H_0^2}{8\pi G}\Omega_m, \tag{4.3.3}$$

where the tilda indicates a dimensionless variable, x_0 is the length of a cell in the grid, H_0 is the current Hubble constant, $\mathbf{p}$ is the particle momenta and Ω_m is the matter density.

The equations solved by the code to compute the potential and the motion of the particles are given by

$$\frac{d\tilde{\mathbf{p}}}{da} = -F(a)\tilde{\nabla}\tilde{\phi}, \qquad \frac{d\tilde{\mathbf{x}}}{da} = F(a)\frac{\tilde{\mathbf{p}}}{a^2}, \tag{4.3.4}$$

$$\tilde{\nabla}^2\tilde{\phi} = \frac{3}{2}\frac{\Omega_m}{a}\,(\tilde{\rho} - 1)\,, \tag{4.3.5}$$

being $F(a)$

$$F(a) \equiv H_0/a = \left(\frac{\Omega_m + \Omega_{curv}a + \Omega_\Lambda a^3}{a}\right)^{-1/2}. \tag{4.3.6}$$

Eqs (4.3.4) and (4.3.5) are solved using a step in space $\Delta x = \Delta y = \Delta z = 1$ and a constant step in the expansion parameter Δa. Thus, by defining the original and the final redshift, and the desired step in the expansion parameter the number of steps the code will run are determined, since $a(t) = (1+z)^{-1}$.

4.3.2 Initial Conditions

The code uses the Zeldovich approximation to set the initial conditions of the simulation. In this approach the relation between the commoving and the lagrangian coordinates is given by

$$\mathbf{x} = \mathbf{q} - \alpha\sum_{\mathbf{k}} b_{|k|}(t)\mathbf{S}_{|k|}(\mathbf{q}), \qquad \mathbf{p} = -\alpha a^2\sum_{\mathbf{k}} b_{|k|}(t)\left(\frac{\dot{b}_{|k|}}{b_{|k|}}\right)\mathbf{S}_{|k|}(\mathbf{q}), \tag{4.3.7}$$

where $\mathbf{S}$ is the displacement vector related to the velocity potential Φ and the power spectrum $P(k)$ by

$$\mathbf{S}_{|k|}(\mathbf{q}) = \nabla_q\Phi_{|k|}(\mathbf{q}), \qquad \Phi_{|k|} = \sum_{\mathbf{k}} a_{\mathbf{k}}\cos(\mathbf{kq}) + b_{\mathbf{k}}\sin(\mathbf{kq}), \tag{4.3.8}$$

being a and b gaussian random numbers with the mean zero and dispersion $\sigma^2 = P(k)/k^4$:

$$a_{\mathbf{k}} = \sqrt{P(|k|)}\frac{Gauss(0,1)}{|k|^2}, \qquad b_{\mathbf{k}} = \sqrt{P(|k|)}\frac{Gauss(0,1)}{|k|^2}. \tag{4.3.9}$$

As it can be seen from Eq. (4.3.9) the random numbers depend on the power spectrum, hence $P(k)$ is very important when calculating the initial conditions. The power spectrum is computed by the code using the following expression:

$$P(k) = \frac{k^n \exp(P_1)}{(1 + P_2 k^{1/2} + P_3 k + P_4 k^{3/2} + P_5 k^2)^{2P_6}}, \tag{4.3.10}$$

where P_i are numerical parameters obtained from a Boltzman code (Boltzman 1989). The exact procedure the code calculates the power spectrum is explained in Chap. 5, hence it will not be presented now.

Nevertheless, it is important to point out that in order to set the initial conditions, and therefore run the simulations, those initial parameters coming from the Boltzman code are needed. Thus, the package that provides the Klypin and Holtzman code includes a file where those parameters appear for a range of different cosmological parameters e.g. the density parameters and the Hubble constant. However, not all the cosmological parameters are changed and even if they are modified, not always present the desired values, presenting this problem the baryonic matter density and the Hubble constant. Thus, there are no values in the file to generate the initial power spectrum, which will define the density distribution at the initial redshift.

A way for solving this problem would be to generate a new set of initial conditions that contained the desired scenario e.g. different values of Ω_b. For doing it, there are different codes available to prepare the initial conditions that would be used as inputs in the simulations. One of those codes is the called COSMIC package, developed by Bertschinger (1995), which contains different FORTRAN programs that generate the initial power spectrum. In order to obtain the initial power, firstly it is necessary to run the LINGER code that calculates the linear evolution of fluctuations generated in the early Universe. The results obtained are then introduced in the GRAFIC program (Gaussian Random Field Initial Conditions), the one responsible to calculate the power spectrum that later will be used as the initial power of the simulations.

However, running these codes needs a large amount of computational resources. Moreover, the outputs of these programmes are in a different format than the inputs of the Klypin and Holztman's code, hence it would be very difficult to import these results as the initial conditions and would require too much time to match them. Taking into account the limits of this thesis in terms of time, resources and objectives, finally was decided that was preferable to quit this part and focus in other fields of the work. Nevertheless, it is important to say that testing the influence of those parameters e.g. baryonic matter versus dark matter, would be an interesting study, and even if it has not been made here it could be done in future projects.

4.3.3 Halo Finder

The algorithm used to find the halos is a *bound-density-maxima* code (BDM) developed by Klypin & Holtzman (1997), which tries to solve some problems appeared in previous programs e.g problems with the satellite galaxies. The BDM code works in two main steps: firstly it finds the center of the halos, and secondly it determines the particles forming those halos.

Explaining in more detail the procedure followed, in the first part the user chooses a radius r_{sp} of a sphere, for which the code will find the center of mass, and the *number of seeds* N_{seed}, that determines the number of spheres with radius r_{sp} that will be placed in the simulation. Thus, every $N_{particles}/N_{seed}$ a sphere will be located and the center of mass found. Then the center of the sphere is moved to the center of mass and the new center is calculated. The process is repeated until the results converge. Besides, additional "seeds" are added in the low-density zones. A characteristic of this part is that halos can have radius larger or smaller that r_{sp}, but distances between halos can never be smaller than r_{sp}. When two different initial spheres find the same halo one of them is the *duplicate* of the other one, and it is removed in order to not have redundant halos.

Once the centers of halos are found, the code establishes which particles belong to each halo. Spherical concentric shells are placed around its center, and the maximum circular velocity a particle in each shell can have is calculated by

$$V_{max} = \sqrt{\frac{GM(r)}{r}}\Big|_{max}. \tag{4.3.11}$$

At the same time, the escape velocity for a particle at a given radius r is computed using

$$V^2_{escape}(r) \approx (2.15 \cdot V_{max})^2 \frac{\ln(1 + 2r/r_{max})}{(r/r_{max})}, \tag{4.3.12}$$

where r_{max} is the radius of the maximum rotational velocity. Eq. (4.3.12) it is valid when the Navarro-Frenk-White (1997) density profile for the halos is assumed. When a velocity of a particle calculated by Eq. (4.3.11) is larger than V_{escape} the particle is unbound. Nevertheless, as V_{max} and V_{escape} are calculated before the particles are removed, the process cannot be done in one step; hence a reiterative process is applied, where the velocities are calculated many times until the results converge.

4.3.4 List of Files

The following list are the FORTRAN programs included in the Klypin and Holtzman's package, describing their function and utility:

- `PM_to_ASCII.f`: Convert PM format to ASCII.
- `PMhalos.f`: Contains the Bound Density Maxima code to find dark matter halos.
- `PMmain.f`: Run the simulations calculating the density and the potentials.
- `PMmodelCHDM.f`: Introduce the cosmological and the simulation parameters in the code for the Hot+Cold Dark Matter model.
- `PMmodels.f`: Introduce the cosmological and the simulation parameters in the code for the Lambda Cold Dark Matter model.
- `PMpower.f`: Computes the simulated matter power spectrum and the mass variance using the density field values as inputs.

- `PMselect.f`: Selects and scales Particle-Mesh particles.
- `PMstartCDM.f`: Sets the initial conditions for the Lambda Cold Dark Matter model with the values introduced in `PMmodels.f`.
- `PMstartCHDM.f`: Sets the initial conditions for the Hot+Cold Dark Matter model with the values introduced in `PMmodelCHDM.f`.

Chapter 5

Analysis Tools

When studying any kind of data, it is very important to use the correct analysis methods and tools to treat the information. In cosmology, the techniques used to study the formation of large structures in a simulated universe with N-body techniques are usually statistical tools that give information about the simulation considering the variables as signals. The "modes" of the density field are analyzed with statistical procedures, as the power spectrum or the variance. Nevertheless, other relevant information can be obtained from more direct approaches e.g. density plots, which present the data directly obtained from the simulations.

5.1 Density Plots

The most visual method to check the results obtained from the simulations and see how the formation of structures evolve is the plotting of the density field. These plots can be done in 2 or 3 dimensional spaces, and they show the values of the density fluctuations using a colour scale.

In this thesis the density plots have been done in two dimensions, projecting the values of the density field in one plane, hence obtaining a plot showing the structures formed. Thus, it is easier to understand how the system evolves, and a more visual idea of the results calculated by the code can be given. Moreover, the plots used in the thesis are normalized for the largest value and scaled using a logarithmic scale, hence the density plots show the adimensional density fluctuations with the given normalization and scale for each point of the grid simulation, depending this density on the number of particles found in that concrete point of the grid. Nevertheless, these plots do not represent the exact shape of the structures created, since the projection of the density erases the information about the exact position of the density value considered in each location.

Furthermore, the density fluctuations can be calculated for any desired redshifts, then it is possible to compute the density plots for the initial, the final or any other redshift. Therefore it is a good method to compare visually the evolution of the system for different epochs, being able to study the first, the intermediates and the final steps of the simulations.

5.2 Power Spectrum

5.2.1 Linear Power Spectrum

The power spectrum is usually calculated from the results obtained in the simulations, since the evolution of the universe simulated involves non-linear processes that are extremely difficult to describe by analytical expressions. However, it is possible to calculate the power spectrum analytically when only the linear-regime is considered, using the equations that define this region. Respectively, in this thesis the linear matter power spectrum is calculated by the code using linear theory. Thus, the code calculates the linear growth and the transfer function in order to obtain the linear power spectrum for a certain redshift. Nevertheless, the code computes these functions using a special normalization, making not obvious to understand the exact procedure followed. For this reason, the calculations are going to be presented with more detail, taking into account that the ΛCDM model and the HCDM model do not use the same exact equations.

For a more deeply understanding of how the code used in the thesis works, the list of equations and the indications where they can be found in the code is presented in Appendix B.

Lambda Cold Dark Matter Model

Firstly the power spectrum for the original redshift is obtained using

$$P_{ini}(k) = \frac{k^n \exp(P_1)}{(1 + P_2 k^{1/2} + P_3 k + P_4 k^{3/2} + P_5 k^2)^{2P_6}}, \tag{5.2.1}$$

being k^n the primordial power spectrum from the Big Bang, and the rest of the expression is the square of the *Transfer function T(k)*, which is

$$T(k) = \frac{\exp(P_1)}{(1 + P_2 k^{1/2} + P_3 k + P_4 k^{3/2} + P_5 k^2)^{2P_6}}; \tag{5.2.2}$$

hence, the linear power can be expressed as

$$P_{ini}(k) = k^n T^2(k), \tag{5.2.3}$$

where the numerical parameters P_i appeared in $T(k)$ are values obtained using a Boltzman code (Holtzman 1989) that sets the value of the Transfer function and the linear power spectrum for a certain initial conditions.

Once this part of the power spectrum is done, it is necessary to apply the modification due to the growth rate [see Eq. (3.2.15)] of the density instabilities and the normalization parameters. Thus,

$$P_{lin\,\Lambda CDM}(k, a) = \left(\frac{\delta_g(a)}{\delta_g(a_{initial})}\right)^2 P_{ini}(k) S_n h^3 \left(2\pi^2\right) \tag{5.2.4}$$

is the final equation for the linear matter power spectrum, being P_{ini} the power presented above, S_n [see Eq. 5.2.5] is the normalization of the spectrum for the bias parameter using

σ_8 and a Tophat window function $W(x)$, and h is the dimensionless hubble pararmeter. Furthermore, additional constants are used to transform the power into the correct units.

$$S_n = \frac{\sigma_8^2}{\int_{10^{-5}}^{20} W(x)dx} \tag{5.2.5}$$

Hot+Cold Dark Matter Model

The process to compute the linear power spectrum when hot dark matter is included is very similar to the previous case, with the difference that the power spectrum of the hot component has to be calculated. Besides, the grow of the power will be influenced by the quadrupole moment instead of σ_8. Thus, $P_{inicold}(k)$ and $P_{inihot}(k)$ are given by

$$P_{ini\,cold}(k) = \frac{k}{(1 + P_2k^{1/2} + P_3k + P_4k^{3/2} + P_5k^2)^{2P_6}} \tag{5.2.6}$$

$$P_{ini\,hot}(k) = P_{inicold}(k)\frac{k\exp -PP_1k}{1 + PP_2k^{1/3} + PP_3k^{2/3} + PP_4k + PP_5k^{4/3} + PP_6k^{5/3}} \tag{5.2.7}$$

respectively, where P_i and PP_i are are parameters given in the code which sets the initial conditions for a given cosmology. With these expressions is possible to obtain the equations for the power spectrum of the cold and hot dark matter

$$P_{COLD}(k, a) = a^2\Omega_{CDM}^2 P_{inicold}(k)S_n h^3 2\pi^2 \tag{5.2.8}$$

$$P_{HOT}(k, a) = a^2\Omega_{\nu}^2 P_{inihot}(k)S_n h^3 2\pi^2, \tag{5.2.9}$$

being a the expansion factor, Ω_{CDM} the cold dark matter density, Ω_ν the hot dark matter density, S_n the normalization factor and h the dimensionless hubble parameter. In these equations the variation due to the time dependance is given by the expansion factor, since this value is time dependent. On the other side, the normalization factor S_n is calculated in a different manner, being

$$S_n = \frac{Q^2 4\pi}{2\pi^2 5 fact(ns, 2)R_h^{(ns+3)}}. \tag{5.2.10}$$

Here, R_h is the horizon radius and ns the slope of the power spectrum, while Q is obtained from

$$Q = \frac{quadrupole}{2.726K}, \tag{5.2.11}$$

which is the quadrupole moment normalized to the main temperature of the Universe. Finally, the final linear power spectrum is computed using the square sum of these two components, with the final expression

$$P_{lin\,CHDM} = P_{COLD}(k, a) + P_{HOT}(k, a) + 2P_{COLD}(k, a)^{1/2}P_{HOT}(k, a)^{1/2}. \tag{5.2.12}$$

5.2.2 Simulated Power Spectrum

The simulated power spectrum is obtained from the density field generated by the simulation, calculated in the Klypin-Holtzman code as

$$P(k) = \frac{1}{L^3} \frac{\sum \left|\hat{\delta}(\mathbf{k})\right|^2}{\Delta N_k}. \tag{5.2.13}$$

This formula computes the average square amplitude of the density fluctuations simulated by the code, where $\hat{\delta}(\mathbf{k})$ is the fast Fourier trasnform of the density field $\delta(\mathbf{x})$, the sum is over the wave-numbers found in a spherical shell of radius k and thickness $2\pi/L$, L is the size of the box simulation, and ΔN_k is the number of harmonics in the shell.

Nevertheless, when using these statistical tools, is important to know where the discreteness effects can appear, in order to prevent the use of wrong data that could disturb the correct results. In the case studied, the limit where the values obtained by the code can be trusted is given by the Nyquist frequency. Any signal with higher frequency than the Nyquist frequency is susceptible to not be reconstructed correctly, since there is not enough sampling points to collect all the information. In a N-body simulation computed with a particle-mesh code, the Nyquist frequency comes from the number of particles used and the size of the box simulated, resulting in

$$k_N = \frac{\pi N}{L}, \tag{5.2.14}$$

where N is the number of particles in one row and L is the size of the box. Therefore any mode with a frequency higher than Eq. (5.2.14) cannot be taken into account in the results, since its values can be affected by the lack of particles when comparing with the size of the universe simulated.

5.3 Mass Variance

The mass variance provides information about the range of values that mass can have when a certain radius is considered. Thus, it shows how large is the uncertainty of the mass value for a structure of a given scale. The mass variance is computed from the simulated power spectrum presented previously using the following equation:

$$\sigma_M^2(r) = \frac{1}{2\pi^2} \int_0^\infty P(k) W^2(kr) k^2 dk, \tag{5.3.1}$$

being $P(k)$ the simulated power spectrum and $W(kr)$ the spherical top-hat window function

$$W(x) = \frac{3}{x^3} \left(\sin x - x \cos x\right). \tag{5.3.2}$$

Since the mass variance is calculated using the power spectrum, the discreteness effects that affect the power also produce problems in the mass variance values. However, the

mass variance is a function of radius, which is in proper length scales, hence the Nyquist frequency is transformed in length units by

$$\lambda = \frac{2\pi}{k}. \tag{5.3.3}$$

Both, the power spectrum and the mass variance, are obtained after the simulation is finished, and are computed by an additional file of the Klypin-Holtzman code, `PMpower.f`. For further understanding of how the code works, the exact methods to calculate these values can be found in that file.

Chapter 6

Simulations

The dark matter simulations have been planned in three categories, which can be classified as the Basic Simulation RUN0, the set of Lambda Cold Dark Matter simulations ΛCDM, and finally the Hot+Cold Dark Matter simulations HCDM. The Basic Simulation uses accepted values for the most important cosmological paramters, while ΛCDM simulations are based in the same model of cosmology than RUN0 but changing the values of some of those parameters. HCDM simulations, on the other side, include a certain proportion of hot dark matter.

As the results are showed, it will be clear the effect of the different components in the Universe e.g. dark matter and dark energy, as well the different constants and parameters that define it e.g. the Hubble constant. Moreover, the consequences of changing those values will be explained, making possible to see how different the Universe would be if these parameters did not have the current values we know.

6.1 The Basic Simulation: RUN0

In this part of the simulations, the cosmological parameters that have been used are the *matter density* Ω_m, the Λ *density* Ω_Λ, σ_8 and the *Scalar Spectral Index* n. However, for all the simulations the *curvature density* Ω_k has been considered zero.

RUN0 starts at redshift $z = 15$ and finishes at $z = 0$, performing the simulations in 469 steps, this is a step length $\Delta a = 0.002$. The number of particles considered is $N = 32^3$, the number of cells $N_{cell} = 128^3$, and density parameters of $\Omega_m = 0.3$ and $\Omega_\Lambda = 0.7$, coming the cosmological parameters from the WMAP studies (Jarosik et al. 2010). The complete list of parameters used in this simulations is found in Table 6.1.

6.1.1 Density Plots

Fig. 6.1.1 shows the density plots of the simulation for the initial and the final redshift, $z = 15$ and $z = 0$ respectively. In the initial state the particles are distributed using the Zeldovich approximation, starting then the simulation through the non-linear regime. At $z = 0$ it can be seen that many structures have form, creating clusters of particles, which represents the clusters of dark matter. Even though the formation of structures is clearly observed, the formation of filaments is not completely defined, being the clusters placed

Parameter	Symbol	Value
Λ Density	Ω_Λ	0.7
Matter Density	Ω_m	0.3
Baryonic Density	Ω_b	0.026
Amplitude Galaxy Fluctuations	σ_8	1
Scalar Spectral Index	n	1
Hubble parameter	h	0.7
Number of particles	N	32^3
Number of cells	N_{cell}	128^3
Number of steps	N_{steps}	469

Table 6.1.1: Parameters used in RUN0

in some groups but still with certain degree of homogeneity. Thus, one can notice some pattern in the plot, but not a real shape of filaments to be recognized, probably due to the lack of particles.

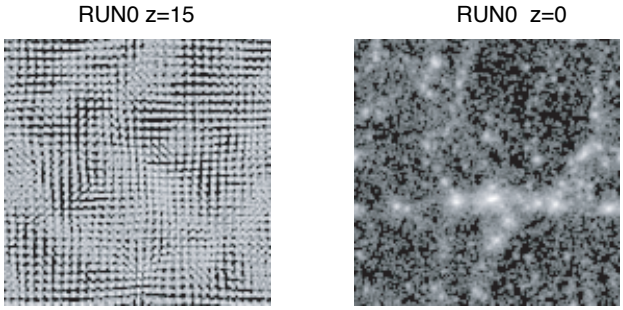

Figure 6.1.1: Density plots for RUN0. The density plots presents the density perturbations projected in one plane, scaled using logarithmic scale and normalized to the largest value

6.1.2 Power Spectrum

In Fig. 6.1.2 the power spectrum obtained from the simulated density field is presented. The solid blue line represents the power spectrum for $z = 15$, while the upper red line is the power spectrum at the present time $z = 0$. Fig. 6.1.2 also includes the Nyquist frequency in order to show the limit where the results of the simulation can be trusted. This is rather obvious for $z = 15$, where once the Nyquist frequency (in this case wavelength) is crossed, there is a very large increase of the power and then a smoother decrease. Moreover, in this part of the curve some peaks and fluctuations can be observed. At $z = 0$ these behaviour is not seen, but as in the previous case the results cannot be taken into account due to the discreteness effects.

Thus, for both redshifts the power spectrum has a similar shape, with more power at large scales (low values of k) than at smaller scales. At $z = 0$ the power spectrum is way

larger than at $z = 15$, since after all the time the simulation has been evolving and the density fluctuations have been increasing, hence many structures have formed in this time. However, the power has not increase at the same rate for all the scales, presenting a lightly higher increase for the small scales than for the larger ones.

On the other side, Fig. 6.1.3 shows the matter power spectrum for the simulation compared with the calculated linear power spectrum. At $z = 15$ the simulated spectrum and the linear one agree very well for all the scales considered, but at $z = 0$ this agreement is much worse. This happens because at $z = 15$ the particles distribution follows the Zeldovich approximation, which belongs to the quasi-linear regime, while at $z = 0$ the system has evolved through the non-linear regime, where the linear-regime equations do not work. Thus, at $z = 0$ the simulated power spectrum is larger than the calculated one, and only at sufficient large scales some match between them can be found. This occurs because at those scales, the modes of the density fluctuations are inside the linear regime, hence they can be predicted by the linear theory. An evidence that the linear theory can be used at that range of wavelengths can be found in the mass variance plot [see Fig. 6.1.4], where it can be seen that at those scales σ^2 is less than one [see Eq. (3.2.4)].

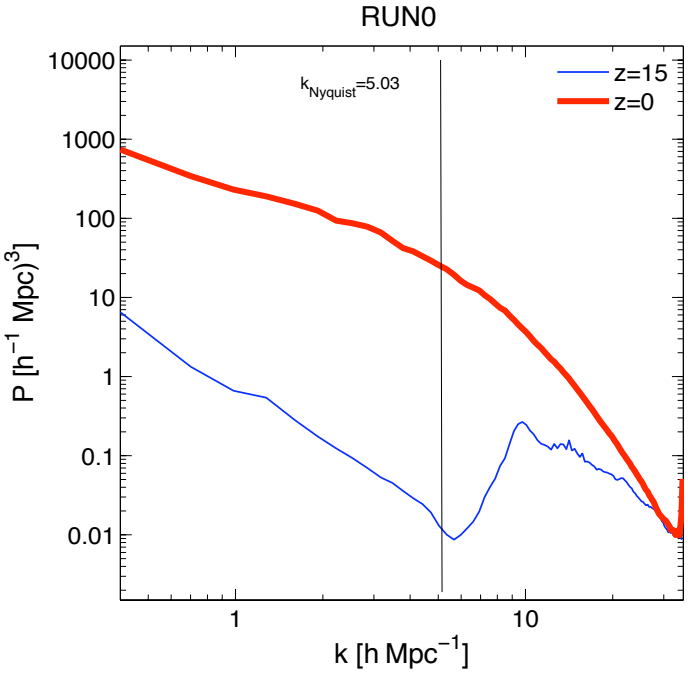

Figure 6.1.2: Matter Power Spetrum for RUN0. Solid blue line represent $z = 15$, while upper red line is $z = 0$

6.1.3 Mass Variance

Fig. 6.1.4 shows the mass variance as a function of radius for $z = 15$ and $z = 0$. In this figure the scales are represented in normal length scales, hence the Nyquist frequency is found at r=1.25. Thus, values at radius smaller than this value may be wrong and cannot be taken into account. Moreover, as the radius increase, the slope of the function varies, approaching the r^{-4} behaviour expected from a grid distribution (Hansen et al. 2007).

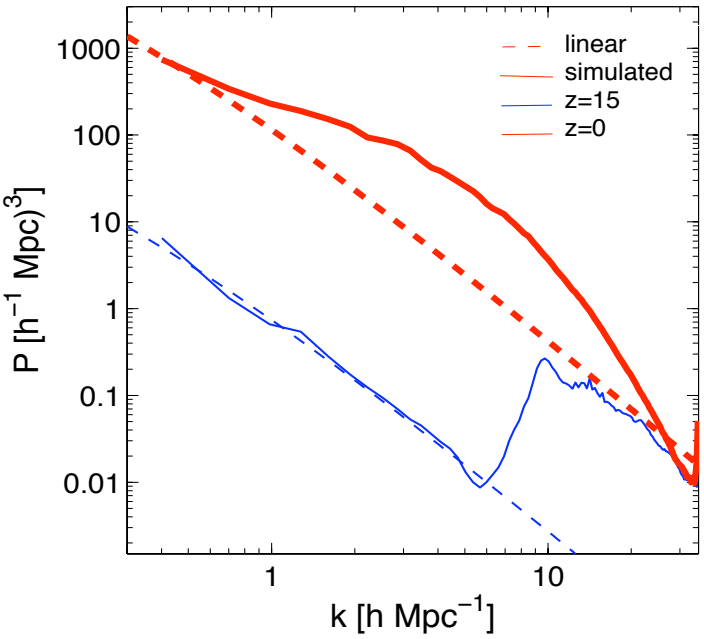

Figure 6.1.3: Matter Power Spetrum for RUN0 vs Linear Power Spectrum. Dashed lines represents the power spectrum calculated using linear theoy, while solid lines are the power spectrum obtained in the simulation. Blue lines show $z = 15$ and red lines $z = 0$

Besides, the mass variance decreases for larger radius, since the distribution of matter is more homogeneous as the scale considered increase. When comparing both redshifths, the variance at $z = 0$ is larger, due to the formation of structures that leads to more inhomogeneity in the matter distribution.

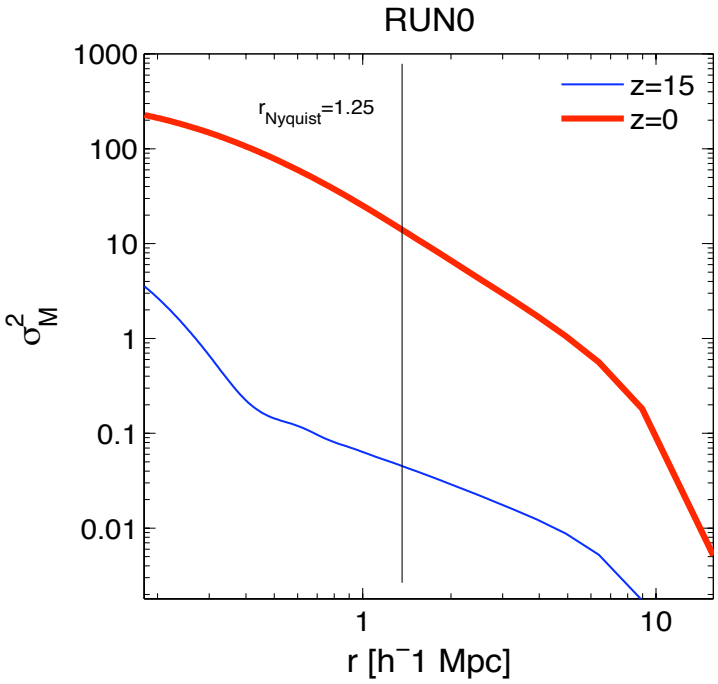

Figure 6.1.4: Mass Variance for RUN0. Solid blue line represent $z = 15$, while upper red line is $z = 0$

6.2 Lambda Cold Dark Matter Simulations ΛCDM

The Lambda Cold Dark Matter simulations (ΛCDM) are a set formed by seven different simulations, RUN1 to RUN7, based in the same cosmology model than RUN0. However, some of the cosmological parameters have been changed in order to test their influence and effects in the results. Thus, RUN1 and RUN2 vary the proportion of dark energy and dark matter, RUN3 and RUN4 change σ_8, and RUN5 and RUN6 modify the value of n. Finally, RUN7 is a simulation with the same cosmological parameters than the ones used in the Hot+Cold Dark Matter simulations, except for the fact that does not include any hot dark matter component.

As done in the Basic Simulaion RUN0, these simulation go from $z = 15$ to $z = 0$ in 469 steps. The number of particles and cells considered are the same, $N = 32^3$ and $N_{cell} = 128^3$ respectively. The rest of the parameters change depending on the simulation, having the complete list in Table 6.2.

6.2.1 Density Plots

Fig. 6.2.1 shows the density plots for RUN1 to RUN7, being the plots in the left the density distribution at $z = 15$ and the ones in the right at $z = 0$. Firstly let us analyze RUN1 and RUN2. RUN1 has larger matter density than RUN0 and RUN2, hence the density plots show higher density values for this simulation. This effect is easily observed at $z = 15$, where the particles are initially distributed and Lambda had no time to act. At $z = 0$, the clustering observed is larger than in RUN0, since the process of hierarchical clustering

Simulation	Ω_Λ	Ω_m	Ω_b	σ_8	n	h
RUN1	0.1	0.9	0.026	1	1	0.7
RUN2	0.9	0.1	0.026	1	1	0.7
RUN3	0.7	0.3	0.026	0.5	1	0.7
RUN4	0.7	0.3	0.026	2	1	0.7
RUN5	0.7	0.3	0.026	1	0.5	0.7
RUN6	0.7	0.3	0.026	1	2	0.7
RUN7	0	1	0.075	1	1	0.5
Number of particles			32^3			
Number of cells			128^3			
Number of steps			469			

Table 6.2.1: Parameters used in the ΛCDM simulations

acts faster due to the gravity potential generated by this higher amount of matter. On the other side, RUN2 presents the opposite behaviour than RUN1. This is expected when it is remembered that RUN2 has a much higher Lambda contribution than RUN1. In this case, the clustering appears weaker than before, even though the shape of the structures formed is still the same. This points out that the role of the Lambda component is more a modification of the evolution rate than an element that completely changes the final shape of the system. Furthermore, the new value for the Lambda density in RUN2 it is not as large compared to the one used in RUN0, leading to smaller differences than in the previous case.

RUN3 and RUN4 use the same density parameters than RUN0, while they change σ_8. The value of σ_8 in RUN3 is half of the one set in RUN0, which means the initial density fluctuations are much lower and the matter is more uniformly distributed in space. As a result of it, the density fluctuations in posterior stages are lower as well, and the clustering appeared at $z = 0$ is less important. Moreover, in RUN4 is possible to see how larger values of σ_8 lead to a much stronger structure formation, as it can be observed at $z = 0$. The effect of varying σ_8 can be explained by the fact that the evolution of the system is strongly influenced by this parameter, since the initial density fluctuations given by σ_8 will grow with time creating gravity potentials that will cause the hierarchical clustering. Thus, higher initial fluctuations will result in a more important clustering and more developed structures at the end of the period studied.

In order to understand the nature of σ_8, an extra density plot is presented in Fig. 6.2.2, which shows the density distribution of RUN4 at $z = 6$ compared to RUN0 at $z = 0$. Thus, it can be observed that they are very similar; hence it is possible to conclude that the variation of σ_8 can be understood as an advance in the initial conditions, resulting in the fact that the initial situation for a system with a high σ_8 is a more advanced stage of a simulation that uses a lower value. Thus, high values of σ_8 lead to a more developed final stage for the same period of time simulated. Needless to say this only have consequences in the time development of the system, which will arrive at a more clustered state earlier, but does not have any effect in the shape of the structures formed.

In RUN5 and RUN6 the factor modified is the Spectral Index n. RUN5 has $n = 0.5$,

half of the original one, hence the power spectrum at redshift 15 is less flat, resulting into a less uniform distribution of the power at different scales. Thus, there is much less power at smaller scales and the density fluctuations at those small scales produce lower gravity potentials for creating the large structures. Completely the opposite is the situation of RUN6 with $n = 2$, where the initial density fluctuations at small scales are larger and the clustering can develop more easily to form structures.

Finally, Fig. 6.2.1 shows that RUN7 produce more clustering at $z = 0$ than RUN0. This is due to the fact that the matter density is larger in this last simulation, hence the gravity helps the formation of large structures. At $z = 15$ it can be seen that the density distribution has larger values than the basic simulation. Moreover, the lower value of the hubble parameter used in RUN7 produce less expansion in the Universe; however, this difference with $h = 0.7$ is rather small, so the effect cannot be completely observed.

6.2.2 Power Spectrum

Fig. 6.2.3 shows the matter power spectrum obtained from the simulated density profiles, where the solid blue line represents $z = 15$ and the upper red line $z = 0$. In all the simulations it can be seen that the power increase as density perturbations grow with time, although this increase has not the same rate for all the scales. Thus, as occurred in RUN0 the increase at small scales is smaller than at large scales. Furthermore, the discreteness effects of the simulations can be observed in Fig. 6.2.3, where simulations with higher random motion of particles present less discreteness perturbations, due to the fact that these random fluctuations partially eliminate the discreteness effects thanks to the white contribution they give to the existing noise. This effect appears in RUN1, RUN4 and RUN6.

Analyzing RUN1 and RUN2, firstly it can be seen that at $z = 0$ the power obtained from RUN1 is lightly larger than RUN2 and RUN0, specially at large scales, since RUN1 presents higher clustering in the density plots. On the other hand, at $z = 15$ RUN0, RUN1 and RUN2 have very similar power at large scales, while at smaller distances RUN1 shows more power. Secondly, when considering RUN2, its power spectrum is very similar to RUN0, since Ω_Λ and Ω_m are changed in a small proportion, therefore it is reasonable to assume that RUN2 presents a scenario very similar to RUN0. At both redshifts, the larger value of Ω_Λ results in a lightly lower power in all scales, since Lambda behaves as a "void" pressure that affects the expansion rate of the Universe, but not the small density details. This especial behaviour of Lambda has been explained in Sect. 3.2, where it is shown how larger values of dark energy reduce the growth rate of density inhomogeneities, especially at later times.

For the next simulations, RUN3 and RUN4, RUN3 shows a lower power spectrum than RUN0 for both redshifts, approximately four times lower, while RUN4 presents a power spectrum four times larger than RUN0 does, being these values exactly the square of the variation of σ_8 respect to the value used in RUN0. This can be deduced from

$$P(k) \propto \sigma_8^2 \tag{6.2.1}$$

that describes the relation between the power spectrum and σ_8 (Peacock 1999; Romeo et al. 2008). Besides, higher values of σ_8 lead to larger density perturbations, hence more

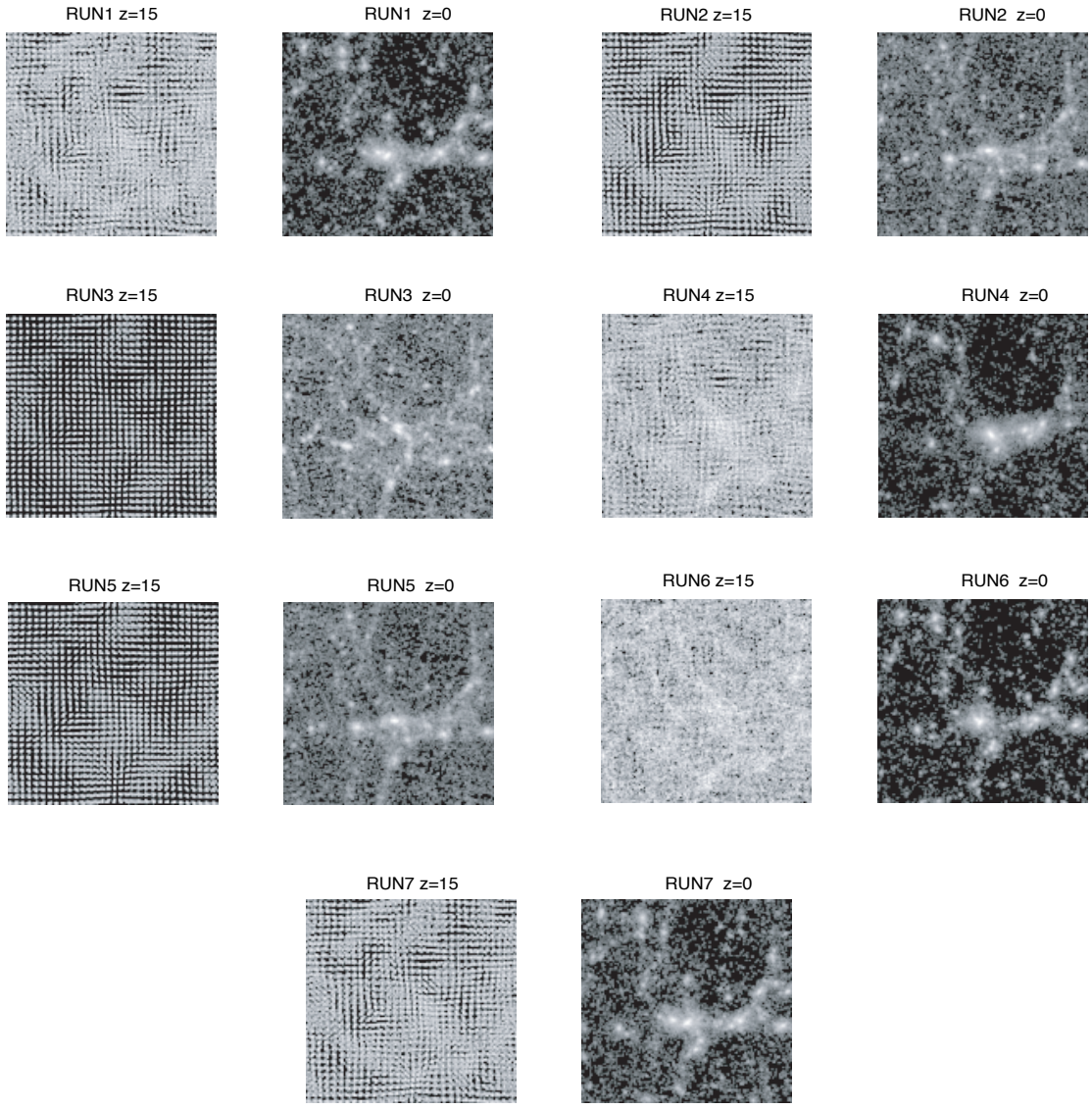

Figure 6.2.1: Density plots for RUN1 to RUN7. The density plots presents the density perturbations projected in one plane, scaled using logarithmic scale and normalized to the largest value

power at $z = 15$. This effect will produce more clustering and structure formation at $z = 0$, which leads to the larger power observed in RUN4 compared to RUN0. The discreteness effects will be reduced as σ_8 increases, due to the higher random motion of the particles, being RUN3 a clear example of how the discreteness effects are very important when σ_8 is rather small.

The power spectrum of RUN5 has lower values than RUN0, because its Spectral Index n is half the original value. Thus, as k increases, the power decreases more comparing with RUN0, meaning less power at smaller scales. RUN6 shows the opposite behaviour, with the power increasing more as higher values of k are considered. Again, the discreteness effects appeared in RUN5 are larger than the ones observed in RUN0 due to the low value of n,

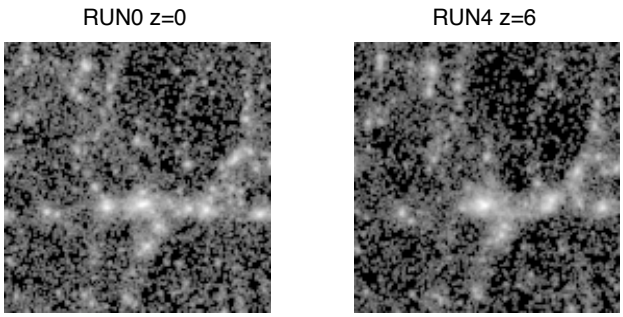

Figure 6.2.2: Density plots for RUN0 at $z = 0$ and RUN4 at $z = 6$. The density plots presents the density perturbations projected in one plane, scaled using logarithmic scale and normalized to the largest value

because the initial density fluctuations at small scales are lower and cannot compensate discreteness problems. However, RUN6 almost eliminate these discreteness fluctuations since the initial density fluctuations at small scales are much larger.

RUN7 presents a power spectrum similar to RUN0 at $z = 15$ and $z = 0$. This may not be expected since RUN7 has no Lambda contribution and changes the hubble parameter compared to RUN0, resulting in the larger clustering observed in the density profiles. Nevertheless, with a more detailed analysis some differences can be found. Thus, at small scales, RUN7 has more power due to the larger Ω_m, being more easily observed at $z = 15$, and it also shows a power with a less stepped profile. At $z = 0$ this is translated in a lightly larger power, especially at small scales, and hence more developed structures.

6.2.3 Mass Variance

Fig. 6.2.4 shows the mass variance for $z = 0$ and $z = 15$. In all the simulations the mass variance decrease as the radius considered increase, pointing out that the Universe becomes more homogeneous at larger scales, agreeing the Cosmological Principle. Thus, RUN1 and RUN2 present a mass variance very similar to RUN0, having RUN1 higher values at small radius. RUN2 is even more similar to RUN0 than the previous case, since both simulations have almost the same cosmological parameters.

Considering RUN3 and RUN4, the mass variance varies with the same proportion than σ_8

$$\sigma_M \propto \sigma_8 \tag{6.2.2}$$

due to the fact that both values represent the variation of mass for a certain dimension, σ_8^2 extrapolated from the linear theory and σ_M^2 in the current studied moment. Thus, RUN3 has a mass variance half of RUN0 and RUN4 two times larger. Furthermore, as it has seen before, lower σ_8 leads to larger discreteness effects, and hence more irregularities in the middle part of the mass variance in RUN3 than in RUN0. Oppositely, in RUN4 these disturbances are minimum.

RUN5 shows lower values of mass variance than RUN0, being this difference larger at small scales, while the variance of RUN6 is larger than RUN0, again more obvious at small

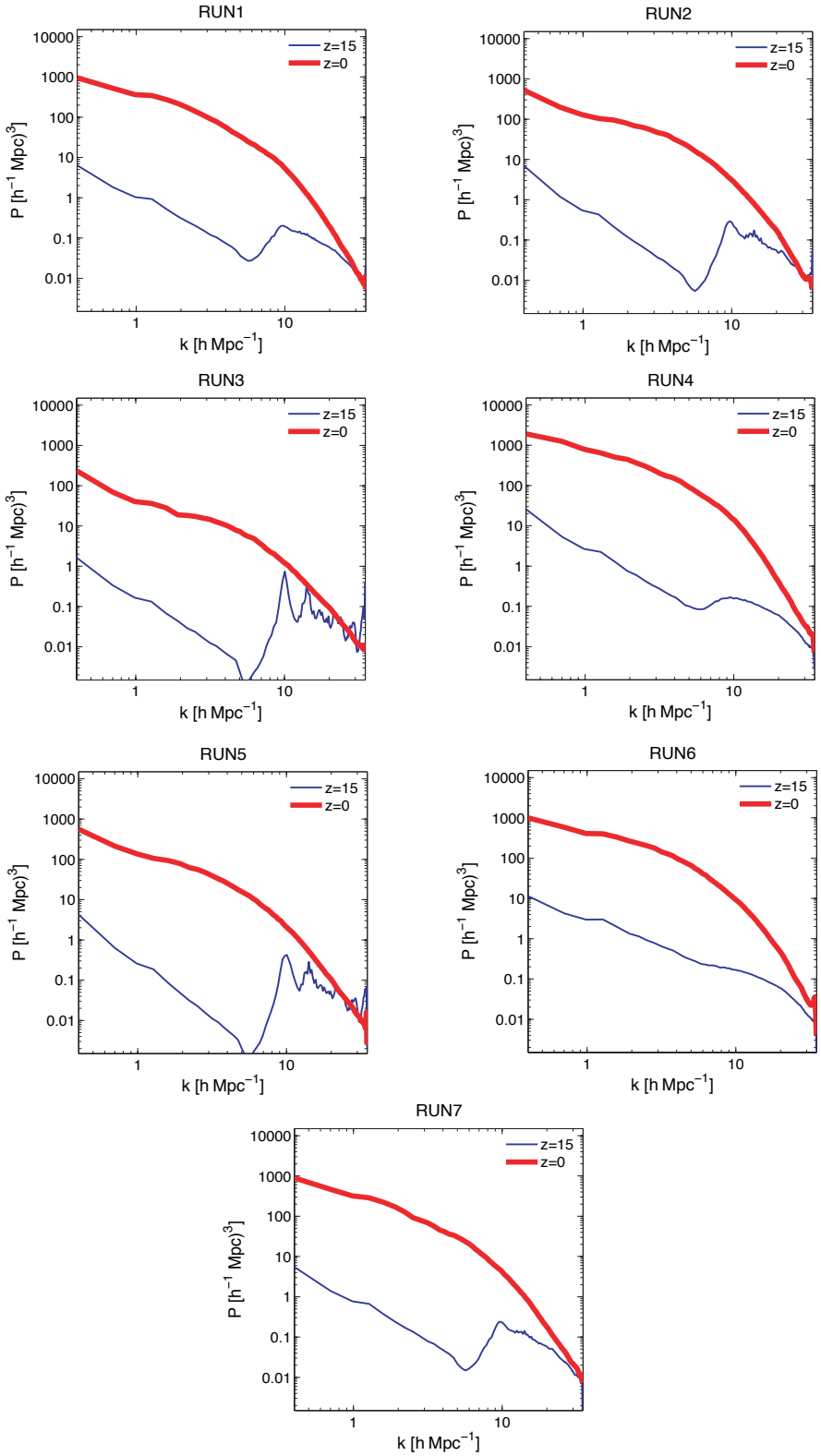

Figure 6.2.3: Matter Power Spetrum for RUN1 to RUN7. Blue solid lines represent initial redshift $z = 15$, upper red lines final redshift $z = 0$

radius. The parameter modified in these simulations is the responsible of this behaviour, since n changes the slope of the power spectrum, and therefore the mass variance changes are not the same depending on the scale considered. The discreteness effects can be seen easily in RUN5; however in RUN6 are very reduced, as it has been seen in the power spectrum analysis.

The last of the ΛCDM simulations, RUN7, has higher values of mass variance than RUN0, being possible to observe the difference at $z = 0$ and $z = 15$ as well. Moreover, the mass variance of RUN7 decreases at a slower rate than RUN0, meaning that the inhomogeneities survive in higher grade at large radius. Thus, all these factors agree with the more developed clustering seen in the density plots for $z = 0$, and the larger density perturbations at $z = 15$.

6.3 Hot+Cold Dark Matter Simulations

The last group of simulations performed are based in a cosmology including hot and cold dark matter. Thus, the Hot+Cold Dark Matter model (HCDM) considers the presence of two different types of dark matter, the cold component and the hot one. Moreover, new cosmological parameters are introduced in these simulations, since the hot dark matter model needs new information in order to set its characteristics. The new parameters required by the code when doing these simulations are the *Hot Dark Matter density* Ω_ν, the *Quadrupole moment*, the *Number of netrino species* and the *Overdensity* δ_c. In all the simulations the amount of hot dark matter has been assumed the same, in this case 20% of the total density of the Universe. The overdensity δ_c is defined as the overdensity of a uniform spherical overdense region at the point at which the exact non-linear model predicts that it should collapse to a singularity, and its value is assumed to be 1.686 (e.g. Eke et al. 1996). Similarly, the number of species remain constant, being its value 2 (Kyplin & Holtzman 1997). On the other side, the quadrupole moment has been the only value modified in these simulations.

Thus, the main difference when comparing these simulations with the ΛCDM models is the presence of hot dark matter. Hot dark matter affects the matter power distribution, since hot dark matter presents a cut-off in its power spectrum at small scales caused by the free-streaming effect. The *free-streaming* is a process when a particle can propagate without scattering. In the hot dark matter case, this occurred when the neutrinos became non-relativistic at very early times, traveling then without scattering with matter. However, before that happened, neutrinos where interacting with matter, erasing all the density fluctuations that had entered the horizon at those time. Since this was at a very young age in the Universe, the only density perturbations inside the horizon radius were those with small scales. Thus, hot dark matter erased small fluctuations that otherwise would have generated density perturbations at later times. Fig. 6.3.1 shows this cut-off of the hot dark matter density in its power spectrum at small scales, while cold dark matter has a much more constant profile.

Besides, this part of the code calculates σ_8 in a different manner than the previous case i.e. in the ΛCDM simulations σ_8 is introduced manually by the user while in the HCDM is calculated by the code. Hence, the effect of varying the quadrupole moment is the modification of σ_8, and as it has been seen previously, this parameter affects in large

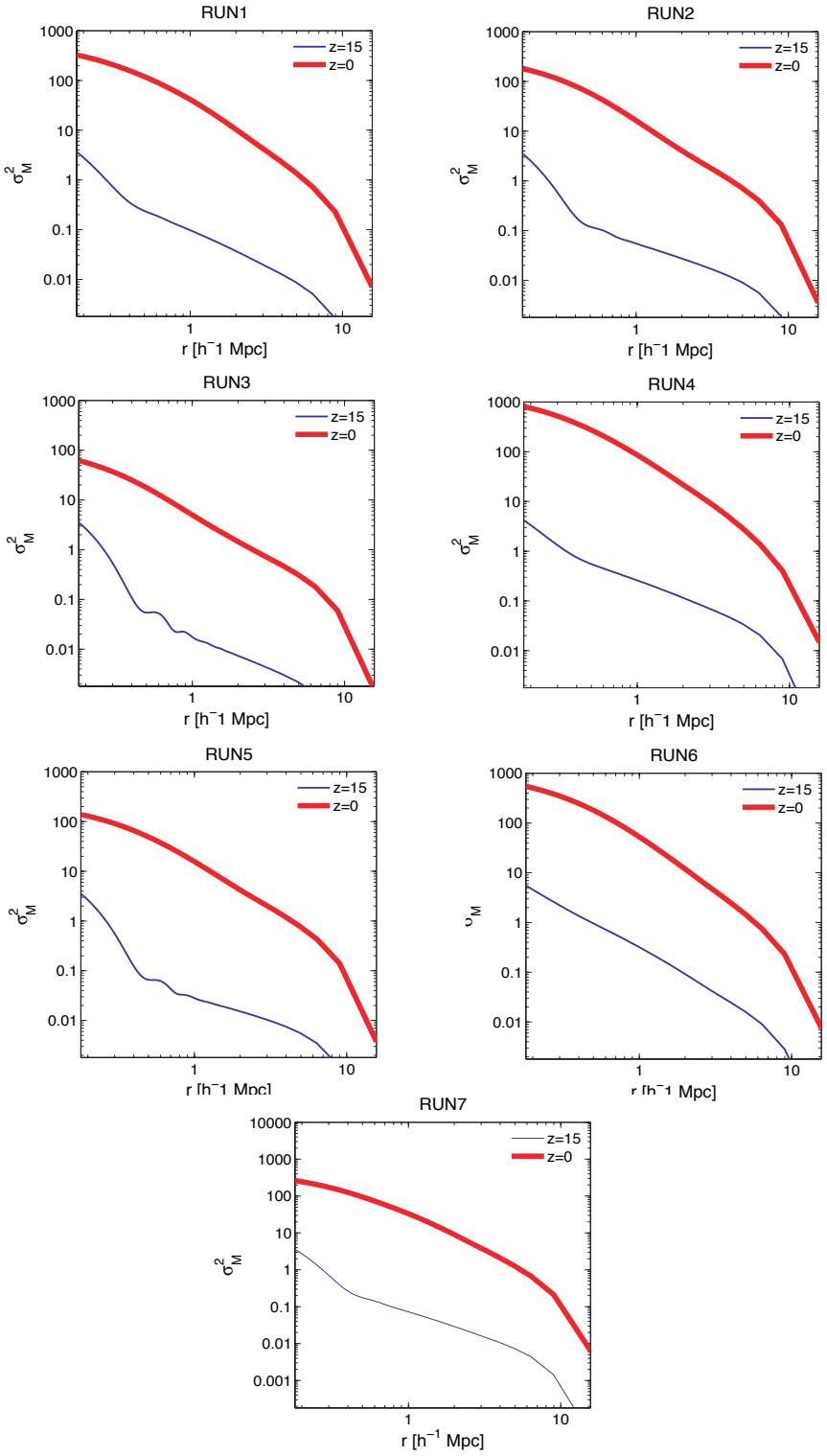

Figure 6.2.4: Mass Variance for RUN1 to RUN7. Blue solid lines represent initial redshift $z = 15$, upper red lines final redshift $z = 0$

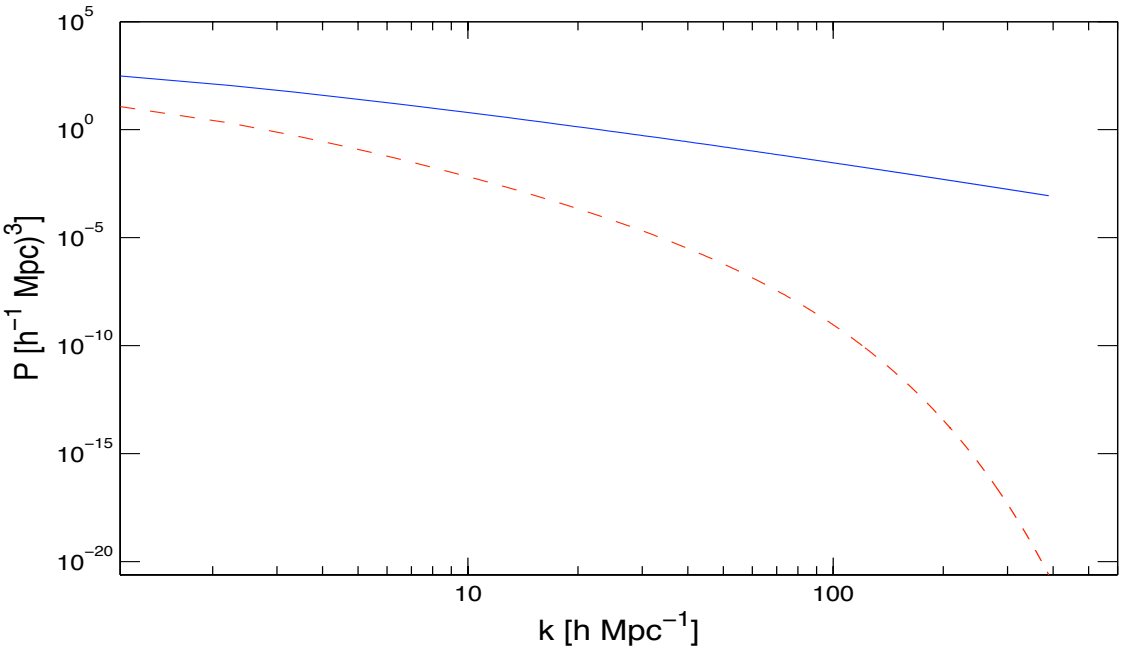

Figure 6.3.1: Matter power spectrum for Hot and Cold Dark Matter calculated using linear theory [Eqs (5.2.8) and (5.2.9)]. Solid blue line represents the Cold Dark Matter and the dashed red line Hot Dark Matter

proportion the results obtained.

The final parameters used in the simulations are presented in Table 6.3, where the values for the quadrupoles are restricted by different reasons. Thus, RUNH1 takes it from the study of the Cosmic Microwave Background Radiation (Jarosik et al. 2010), RUNH2 and RUNH3 have values to test the effect of the quadrupole moment, and RUNH4 has a quadrupole moment that through the equations used by the code will obtain the same σ_8 than RUN0, this is equals 1. In these simulations, the initial redshift is $z = 30$, and the simulations stop at $z = 0$. This is done in 484 steps, being the step length $\Delta a = 0.002$. The number of particles and the number of cells remain constant, being $N = 32^3$ and $N_{cells} = 128^3$.

Simulation	Ω_Λ	Ω_ν	Ω_m	Ω_b	n	h	Quadrupole	δ_c	n°species
RUNH1	0	0.20	1	0.075	1	0.5	14.04	1.686	2
RUNH2	0	0.20	1	0.075	1	0.5	5	1.686	2
RUNH3	0	0.20	1	0.075	1	0.5	100	1.686	2
RUNH4	0	0.20	1	0.075	1	0.5	25.7	1.686	2
				Number of particles		32^3			
				Number of cells		128^3			
				Number of steps		484			

Table 6.3.1: Cosmological parameters used in HCDM simulations

6.3.1 Density Plots

Fig. 6.3.2 shows the density plots for the HCDM simulations, being the left plots the density distribution at $z = 30$ and the right plots at $z = 0$. At $z = 30$ the density fluctuations are very small for RUNH1 and RUNH2, while for RUNH3 are much larger. This is translated to less or more developed structures at $z = 0$, depending on how large were the fluctuations at the oldest redshift. Thus, RUNH2 presents the less evolved scenario, RUNH1 a more clustered one and RUNH3 the most developed structures of all the HCDM simulations. In RUNH1 some structures in the form of clusters can be observed, however is in RUNH3 where this clustering is extremely developed.

On the other side, in RUNH2 the evolution of structures is almost imperceptible. As pointed out before, this is due to the quadrupole moment value. Thus, RUNH3, which has the largest quadrupole moment, has a very large σ_8, while RUNH2 presents a σ_8 much lower.

Finally RUNH4 shows a density similar to RUN7, since both simulations have the same cosmological parameters, being the only difference the small proportion of hot dark matter in RUNH4 compared to RUN7. However, it can be observed that the hot dark matter component decreases the final clustering appeared in the simulation, since the density fluctuations at small scales were erased in some degree, not allowing the creation of larger gravity fields to enhance the hierarchical clustering.

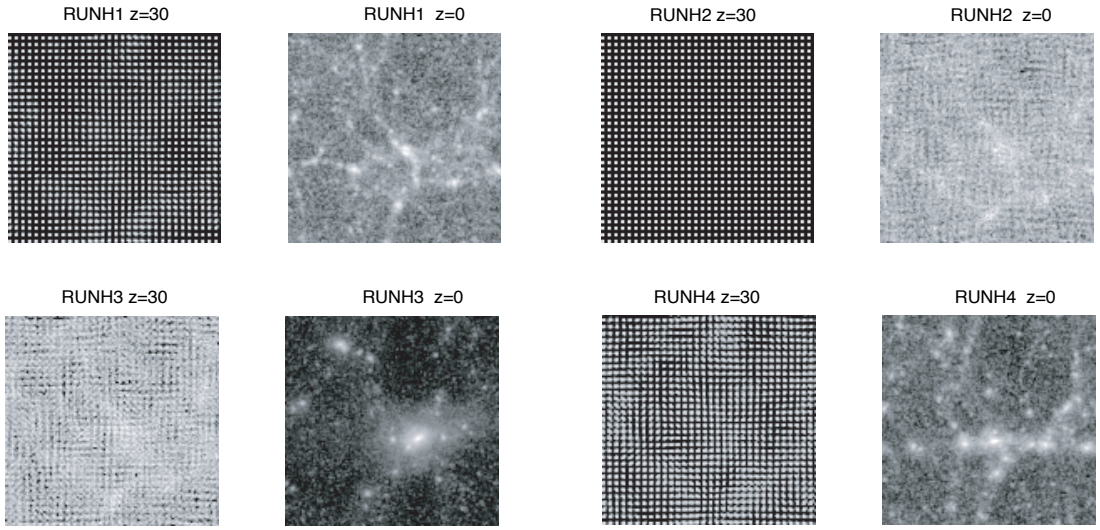

Figure 6.3.2: Density plots for RUNH1 to RUNH4. The density plots presents the density perturbations projected in one plane, scaled using logarithmic scale and normalized to the largest value

6.3.2 Power Spectrum

Fig. 6.3.3 shows the matter power spectrum of the HCDM simulations for the initial redshift $z = 30$, the intermediate redshift $z = 15$ and the final epoch $z = 0$. As it can be expected from the density plots, RUNH2 presents the lowest power spectrum for all the redhsifts,

being RUNH3 the simulation with largest values. On the other side, RUNH1 and RUNH4 have values inside the range formed by RUNH2 and RUNH3. These differences in the power spectrum are related to the quadrupole moment of each simulation, since this value directly affects the σ_8 used by the code. Moreover, in all the simulations there is an obvious decrease in the power spectrum at small scales, approximately at $k = 6$, due to the cut-off in the hot dark matter power spectrum, which produces lower density perturbations at small scales.

Furthermore, it can be seen that larger values of power reduce the discreteness effects that come from the number of particles and the grid resolution, which appear as peaks and irregularities at large values of k. Thus, RUNH2 has very large peaks and perturbations, due to its low quadrupole value, while RUNH3 presents almost no discreteness effects.

Fig. 6.3.4 shows the comparison of the power spectrum between RUNH4 and RUN7, where the dashed lines represents RUNH4, the solid lines RUN7, being the lower blue set at $z = 15$ and the upper red $z = 0$. Important to remember that these two simulations use the same cosmological parameters, being the only difference the proportion of hot dark matter introduced in RUNH4, hence both simulations have the same σ_8 value, even if it is calculated with different methods. Thus, it can be observed that RUNH4 presents lower power spectrum than RUN7. At $z = 0$ the difference seems approximately constant for all the scales. However, at $z = 15$ the power spectrum of RUNH4 is clearly lower at small scales, being more similar to RUN7 at large scales. This is due to the free-streaming process explained previously, which erases the density perturbations at small scales.

6.3.3 Mass Variance

Fig. 6.3.5 shows the mass variance for the four HCDM simulations at three redshifts, $z = 30$, $z = 15$ and $z = 0$. Similarly to the power spectrum study, RUNH3 has the largest mass variance values for the all HCDM simulations, while RUNH2 has the lowest ones. RUNH1 and RUNH4 present the intermediate situations, with σ_8 values of 0.547 and 1 respectively.

It is precisely with RUNH1 and RUNH4 where the effect of σ_8, hence the quadrupole moment can be seen more easily. RUNH4 has σ_8 almost double than RUNH1, showing at the same time a mass variance approximately double than RUNH1. This can be explained remembering that σ_8 is proportional to the mass variance [see Eq. (6.2.2)]. Moreover, it is seen again that larger values of σ_8, which is translated in more important random motion of the particles, reduce the discreteness effects.

Fig. 6.3.6 shows the mass variance of RUNH4 compared to RUN7, being the dashed lines RUNH4 and the solid lines RUN7. RUN7 has lightly larger values of mass variance, specially at small scales, since the density perturbation, and hence the power spectrum of RUNH4, are less important at those radius. However, when large scales are taken into account, these differences almost disappear.

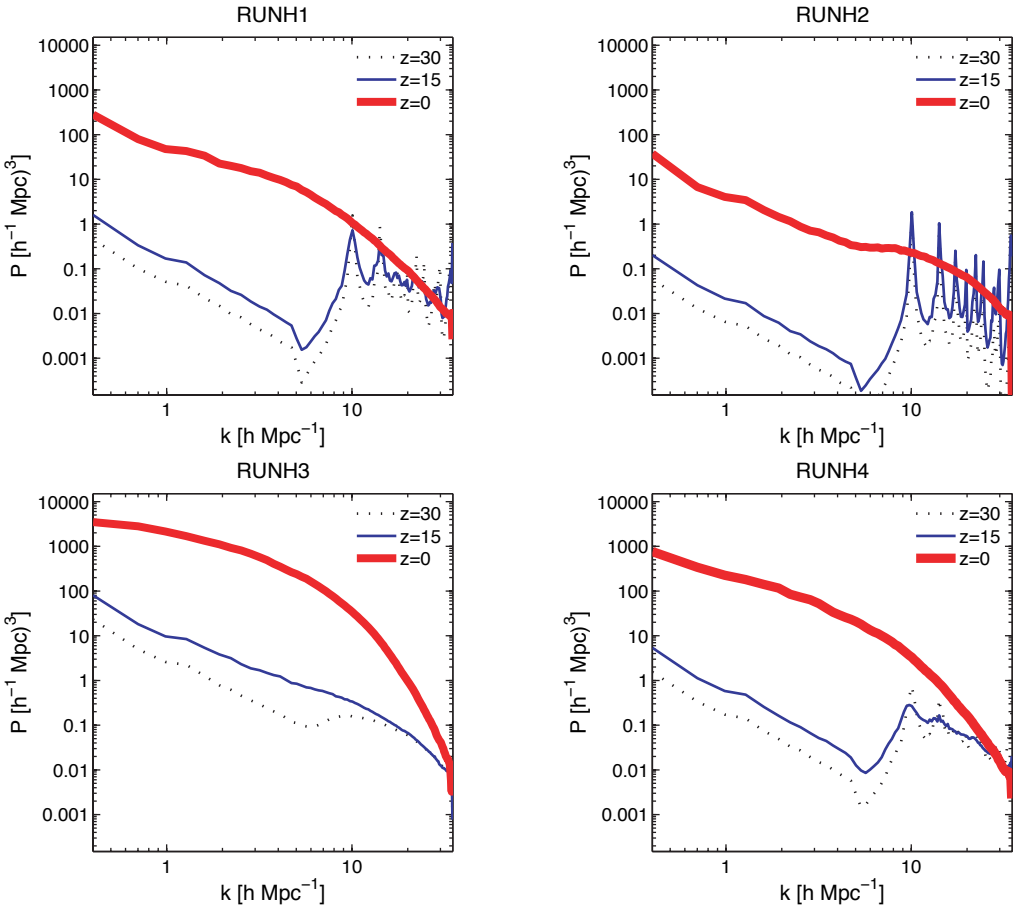

Figure 6.3.3: Matter Power Spetrum for RUNH1 to RUNH4. Dark dotted lines represent initial redshift $z = 30$, blue solid lines $z = 15$ and upper red lines final redshift $z = 0$

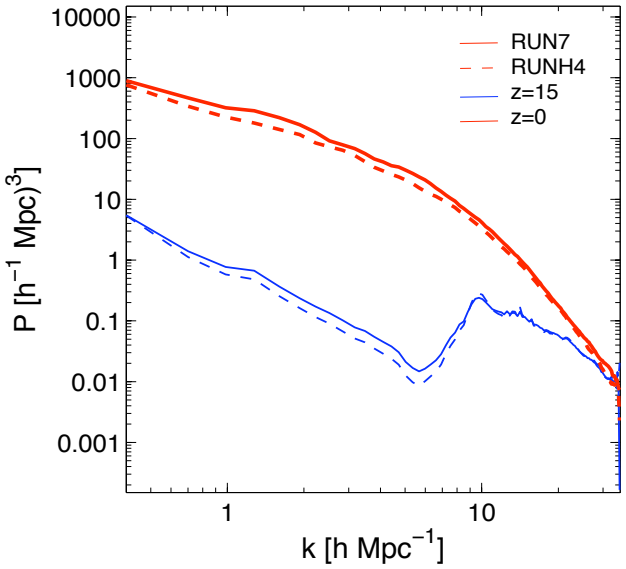

Figure 6.3.4: Matter Power Spetrum for RUN7 vs RUNH4. Solid lines represent RUN7 and dashed lines RUNH4, while the lower blue color is for $z = 15$ and upper red for $z = 0$

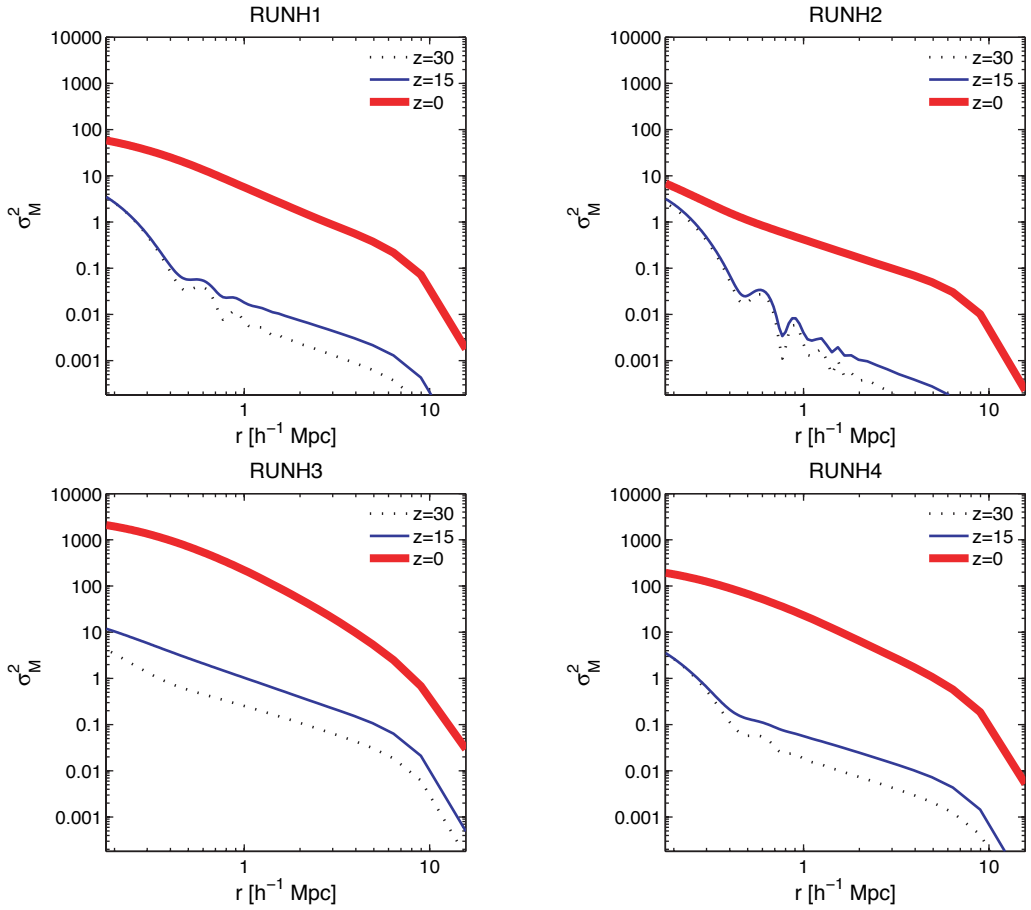

Figure 6.3.5: Mass Variance for RUNH1 to RUNH4. Dark dotted lines represent initial redshift $z = 30$, blue solid lines $z = 15$ and upper red lines final redshift $z = 0$

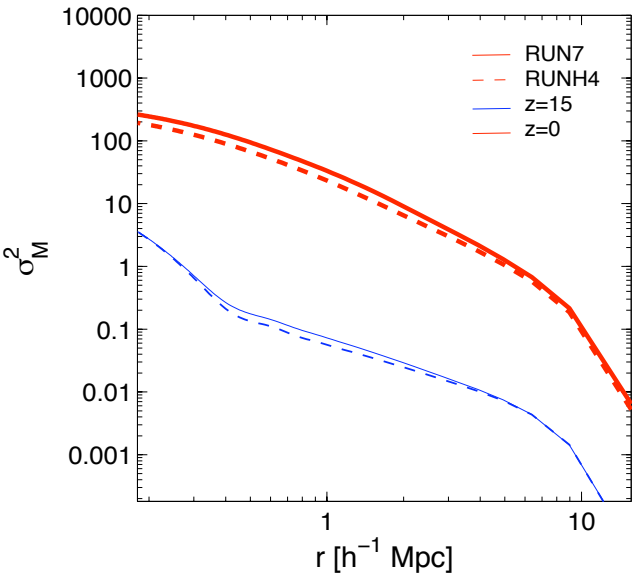

Figure 6.3.6: Mass Variance for RUN7 vs RUNH4. Solid lines represent RUN7 and dashed lines RUNH4, while the lower blue color is for $z = 15$ and upper red for $z = 0$

Chapter 7

Conclusions

In this thesis the effect of the different cosmological parameters have been studied using N-body simulations to represent the formation and evolution of structures in the Universe. After the basic simulation RUN0, two sets of simulations have been performed, testing the effects of the cosmological parameters for the ΛCDM and the HCDM model. This has allowed not only the study of paramaters such as Ω_m, Ω_Λ or σ_8, it has made possible to compare cosmologies with and without hot dark matter as well. Thus, the conclusions achieved with the thesis can be classified as the effects of the cosmological parameters and the effects due to the presence of hot dark matter.

Effects of the Cosmological Parameters

Regarding the cosmological parameters, it has been seen that high values of Ω_m lead to more structure formation, since the larger matter density produce larger gravity fields, which through hierarchical clustering show more developed structures at the end of the simulations. On the other side, Ω_Λ enhances the expansion of the Universe, erasing the density fluctuations at small scales, and reduces the formation of structures. The primordial tilt n has a rather appreciable effect, with higher clustering and more structures as n increases, due to the fact that more power is distributed at small scales.

However, the studied parameter that presents a more important effect is σ_8, which determines the amplitude of the density fluctuations at the initial redshift. The results obtained when varying this parameter are very different from each other, showing its large effect in the formation of structures. Thus, large values of σ_8 results in a very developed clustering, and low σ_8 in almost no observed structures. Nevertheless, the shape of the structures formed does not change, only the time rate at which the simulation evolve, hence the universe simulated varies. Therefore it is possible to conclude that σ_8 changes the initial state of the simulation, making the simulation to start in a more or less developed state depending its value. This is easily seen in Fig. 6.2.2.

It is also important to point out the consequences of modifying the value of the quadrupole moment. It has been seen that this value, which comes from the CMBR anisotropy, affects widely the results, due to the fact that the code used for the simulations uses the quadrupole to calculate the σ_8, implying the consequences discussed in the previous paragraph.

Effects of the Hot Dark Matter

Even if the proportion of hot dark matter in the simulations has not been able to be modified as it was desired, it has been enough to test the effects of its presence and study its implications.

HDM has the characteristic of presenting a cut-off in the power spectrum at small scales, meaning the erasing of density fluctuations at those scales. This leads to less structure formation after the Universe evolves, since the small-scale density fluctuations that would be the seeds for later clustering are not present. As a result, the structure formation in the HCDM model is less developed than in the ΛCDM, showing clear differences when the power spectrum is analyzed. Thus, due to the cut-off of HDM, HCDM has lightly less power at small scales than ΛCDM [see Fig. 6.3.4], which leads to the lower clustering observed in the density plots. Nevertheless, since the HCDM model used has a proportion of HDM rather small, the differences observed in the results are not very large.

Future Work

As it has been explained previously, this thesis has been limited in terms of time and resources, hence it has not been possible to do all the analysis and work that could be desired. For that reason it is important to point out some fields that would be interesting to be studied in future projects to complete the work presented here.

Firstly, the limitations due to computational resources could be solved using more advanced computers, making possible to perform simulations with much larger number of particles. This would reduce the discreteness effect appeared in the results, avoiding the disturbances they produce.

Secondly, it will be interesting to test some cosmological parameters that have not been modified in our simulations, especially the proportion of baryonic matter and the amount of HDM compared to CDM, which has been constant in this project. Thus, the effect of other parameters could be studied, and the behavior of the Universe in the presence of purely HDM could be analyzed, leading to better comparisons with ΛCDM models, and therefore better understanding of HDM.

References

[1] Agertz O., *Simulations of Structure Formation in the Early Universe*, 2004, Chalmers University of Technology

[2] Agertz O., Moore B., Stadel J., Potter D., Miniati F., Read J., Mayer L., Gawryszczak A., Kravtsov A., Monaghan J., Nordlund A., Pearce F., Quilis V., Rudd D., Springel V., Stone J., Tasker E., Teyssier R., Wadsley J., Walder R., *Fundamental differences between SPH and grid methods*, 2007, MNRAS, 380, 963

[3] Barnes J., Hut P., *A hierarchical O(N log N) force-calculation algorithm*, 1986, Nature, 324, 446

[4] Bennett C.L., Boggess N.W., Cheng E.S., Hauser M.G., Kelsall T., Mather J.C., Moseley S.H., Murdock T.L., Shafer R.A., Silverberg R.F., Smoot G.F., Weiss R., Wright E.L., *Scientific results from COBE*, 1993, Adv. Space Res, 13, 12, 409

[5] Bennett C.L., *Cosmology from start to finish*, 2006, Nature, 440

[6] Bertschinger E., *COSMICS: Cosmological Initial Conditions and Microwave Anisotropy Codes*, 1995, in press (arXiv:astro-ph/9506070v1)

[7] Coles P., Lucchin F., *Cosmology. The Origin and Evolution of Cosmic Structure*, 2002, John Wiley & Sons

[8] Efstathiou G.E. ,Eastwood J.W., *On the clustering of particles in an expanding universe*, 1981, MNRAS, 194, 503

[9] Eke V.R., Cole S., Frenk C.S., *Using the Evolution of Clusters to Constrain Omega*, 1996, MNRAS, 282, 263

[10] Hansen S.H., Agertz O., Joyce M., Stadel J., Moore B., Potter D., *An alternative to grids and glasses: Quaquaversal pre-initial conditions for N-body simulations*, 2007, ApJ, 656, 631

[11] Holtzman J.A., *Microwave background anisotropies and large-scale structure in universes with cold dark matter, baryons, radiation, and massive and massless neutrinos*, 1989, ApJS, 71,1

[12] Jarosik N., Bennett C.L., Dunkley J., Gold B., Greason M.R., Halpern M., Hill R.S., Hinshaw G., Kogut A., Komatsu E., Larson D., Limon M., Meyer S.S., Nolta M.R., Odegard N., Page L., Smith K.M., Spergel D.N., Tucker G.S., Weiland

J.L., Wollack E., Wright E.L., *Seven-Year Wilkinson Microwave Anisotropy Probe (WMAP) Observations: Sky Maps, Systematic Errors, and Basic Results*, 2010, in press (arXiv:1001.4744v1)

[13] Jedamzik K., Pospelov M., *Big Bang Nucleosynthesis and Particle Dark Matter*, 2009, in press (arXiv:0906.2087v1)

[14] Jing Y.P., Boerner G., Valdarnini R., *Three-point correlation function of galaxy clusters in cosmological models: a strong dependence on triangle shape*, 1995, MNRAS, 277, 630

[15] Kang H., Ostriker J.P., Cen R., Ryu D., Hernquist L., Evrard A.E., Bryan G.L., Norman M.L., *A Comparison of Cosmological Hydrodynamic Codes*, 1994, ApJ, 430, 83

[16] Klypin A., Holtzman J., *Particle-Mesh code for cosmological simulations*, 1997, in press (arXiv:astro-ph/9712217v1)

[17] Klypin A., *Numerical Simulations in Cosmology III: Dark Matter Halos*, 2000, in press (arXiv:astro-ph/0005504v1)

[18] Navarro J.F., Frenk C.S., White S.D.M., *A Universal Density Profile from Hierarchical Clustering*, 1997, ApJ, 490, 493

[19] Ostriker J.P., Steinhardt P., *New Light on Dark Matter*, 2003, Science, 300, no 5627, 1909

[20] Padmanabhan T., *Theoretical Astrophysics. Volume III: Galaxies and Cosmology*, 2002, Cambridge University Press

[21] Peacock J.A., *Cosmological Physics*, 1999, Cambridge University Press

[22] Press W.H., Schechter P., *Formation of galaxies and clusters of galaxies by self-similar gravitational condensation*, 1974, ApJ, 187, 425

[23] Primack J.R., Gross A.K., *Hot Dark Matter in Cosmology*, 2000, in press (arXiv:astro-ph/0007165v1)

[24] Primack J.R., *Whatever Happened to Hot Dark Matter?*, 2001, SLAC Beam Line 31N3, 50

[25] Riess A.G., *The Case for an Accelerating Universe from Supernovae*, 2000, Publ.Astron.Soc.Pac., 112, 1284

[26] Romeo A.B., Agertz O., Moore B., Stadel J., *Discreteness effects in ΛCDM simulations: a wavelet-statistical view*, 2008, ApJ, 686, 1

[27] Roos M., *Expansion of the Universe - Standard Big Bang Model*, 2008, in press (arXiv:0802.2005v1)

[28] Ryu D., Ostriker J. P., Kang H., Cen R., *A cosmological hydrodynamic code based on the total variation diminishing scheme*, 1993, ApJ, 414, 1

[29] Sheth R.K., Tormen G., *Large scale bias and the peak background split*, 1999, MNRAS, 308, 119

[30] Springel V., Frenk C.S., White S.D.M., *The large-scale structure of the Universe*, 2006, Nature, 440

[31] D. M. White, *Inner Space/Outer Space: the interface between cosmology and particle physics*, 1986, University of Chicago Press

[32] Yoshida N., *Structure Formation in the Early Universe*, 2009, in press (arXiv:0906.4372v1)

[33] Zhang W., MacFadyen A.I., *RAM: A Relativistic Adaptive Mesh Refinement Hydrodynamics Code*, 2006, in press (arXiv:astro-ph/0505481v2)

Appendix A

Dark Halos

In this section of the Appendix the results of the dark halos study is presented. They are placed here since this part of the thesis does not belong to the main set of simulations planned at the beginning, hence they do not try to respond the questions presented in the Introduction.

Thus, why the dark halos analysis has been done? The purpose of this study is to use the programs in the code responsible of the dark halos detection, and test the results obtained when different situations are considered. Dark halos have been searched using the *Bound Density Maxima* (BDM) code included in the package released by Klypin & Holtzman (1997), and with the data obtained the number density of halos and the density profile of the biggest halo have been calculated.

The parameter modified when searching the halos has been the number of seeds placed by the code in the simulation box in order to begin the process. These seeds are the center of spheres that are used to determine the mass and the center of mass of a certain region, repeating the procedure until the results converge and the halos are found. The complete explanation of how the BDM code works can be found in Sect. 4.3.3. Trying to understand the effect of the number of seeds e.g. changes in the values or the resolution of the results, three different values for the number of seeds have been used, being them 500, 1000 and 2000.

The search of dark halos has been done using the results obtained from RUN0. Moreover, many other parameters have been set in the code to have a reasonable scenario when searching the halos. Thus, the minimum radius of halos, their minimum mass as well as velocity limits and other parameters are introduced in the program. One of those parameters is the *overdensity* of the halos, which is the needed overdensity to have collapse (Navarro et al. 1997), hence the code requires the minimum value of overdensity that will assure the formation of the structure. The complete list of parameters is presented in Table A.

The method used to test the results is to compare the number density predicted theoretically versus the simulations data, as well as the density profile of the biggest halo found in each simulation.

Parameter	Value
Minimum center overdensity for halos	340
Overdensity threshold for halos	340
Minimum halo mass	$5 \cdot 10^9 h^{-1} M_\odot$
Comoving search radius	$0.050 h^{-1}$Mpc
Smaller radius of final halos	$0.030 h^{-1}$Mpc
Minimum radius for halos	$0.030 h^{-1}$Mpc
Fraction of DM particles	1
Rejection velocity limit	1.0 (V/V_{escape})
Distance to check for velocity duplicate	$0.030 h^{-1}$Mpc
Define duplicate if $(V_1 - V_2)/V_{rms} <$	0.10
Comoving box size	$20 h^{-1}$Mpc
Shell factor	5
Number of seeds	500 - 1000 - 2000
Number of neighbors	100

Table A.0.1: Parameters used in dark halos

A.1 Number Density of Halos

The number density of halos can be calculated theoretically using

$$n(M,z)dM = \frac{\rho_0}{M}\frac{d\nu(M,z)}{dM} f(\nu) dM,$$

where $f(\nu)$ is a mass function, ρ_0 is the mean density of the Universe at $z = 0$, and ν is given by

$$\nu(M,z) = \frac{\delta_c(z)}{\sigma(M,z)}.$$

In the previous equation $\sigma(M,z)$ is the mass variance [Eq. (5.3.1)], which can be related to the mass of the halo by

$$M = \frac{4}{3}\pi R^3 \rho.$$

On the other side, δ_c is the critical overdensity of an uniform spherical overdense region at the point at which the exact non-linear model predicts that it should collapse (e.g. Eke et al. 1996), being its value $\delta_c = 1.686$.

The mass function has been approximated using two methods: the *Press-Schechter* (PS) approximation and the *Sheth-Tormen* (ST) mass function. The PS approximation was proposed by Press & Schechter (1974) and presents the mass function as

$$f(\nu) = \sqrt{\frac{2}{\pi}} \exp\left(-\nu^2/2\right),$$

while the mass function developed by Sheth & Tormen (1999) is given by

$$f(\nu) = \sqrt{\frac{2}{\pi}} 0.2709 (1 - 1.1096\nu^{0.6}) \exp\left(-0.707\nu^2/2\right).$$

Figs A.1.1, A.1.2 and A.1.3 show the number of halos with mass larger than M. For the three number of seeds, all the curves present larger number of halos at large masses than the number expected by the PS and ST approximations. Nevertheless, when $N_{seed} = 2000$ the number of halos found by BDM is higher than the predicted for almost the whole range of masses, only being lower than ST approximation at low masses. This is due to the fact that as the number of seeds increase, the number of halos found, especially with low masses, increase as well. Hence a high N_{seed} gives more accuracy to found small halos that otherwise would be not found and ignored by the BDM code. Furthermore, as the mass considered increases, the number of halos discovered is lower and discreteness effects appear, showing peaks and irregularities in the curves.

It is also interesting to point out the differences between PS and ST approximations. Thus, ST predicts larger number of halos than PS, being this difference bigger for large masses, and reducing it as the masses taken into account decrease.

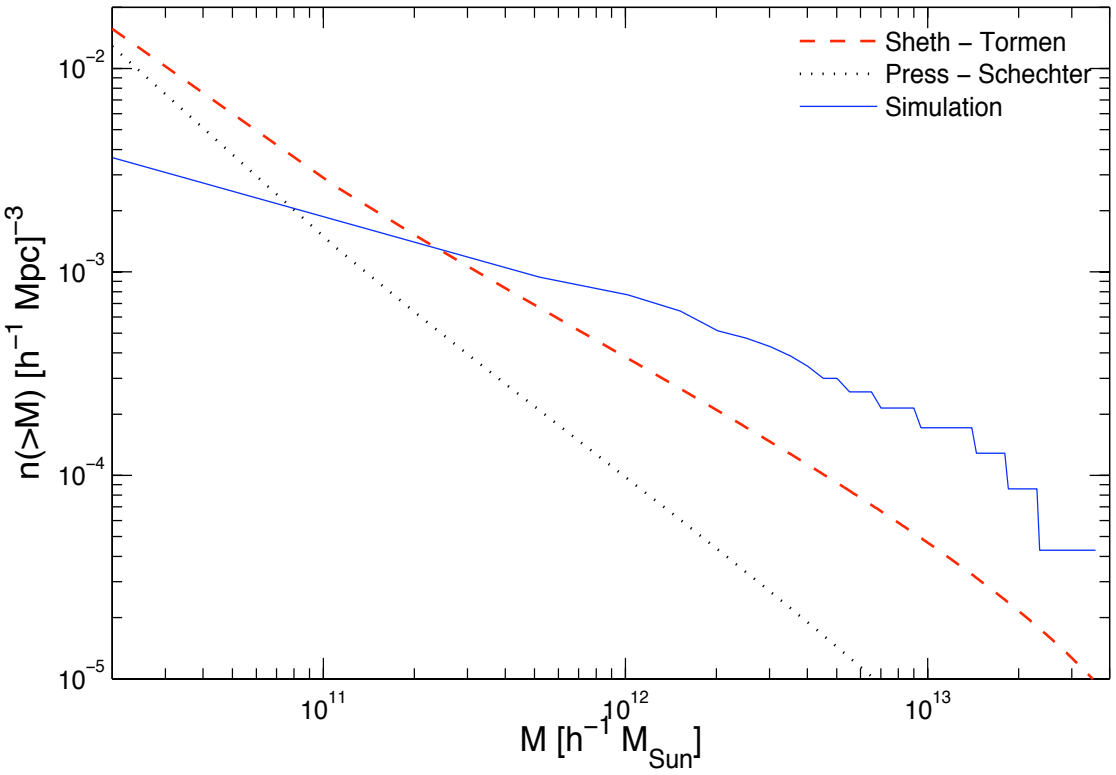

Figure A.1.1: Number density of halos with mass larger than M for $N_{seed} = 500$. The solid blue line are the halos found by BDM code, while the upper dashed line is the ST approximation and the lower dotted black line is the PS approximation

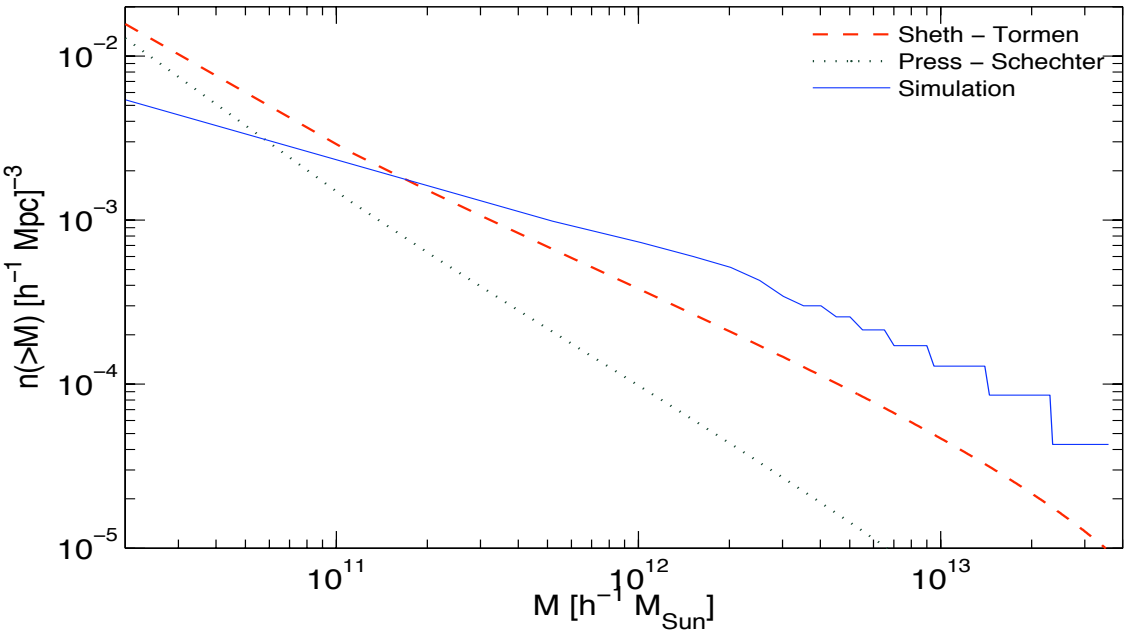

Figure A.1.2: Number density of halos with mass larger than M for $N_{seed} = 1000$. The solid blue line are the halos found by BDM code, while the upper dashed line is the ST approximation and the lower dotted black line is the PS approximation

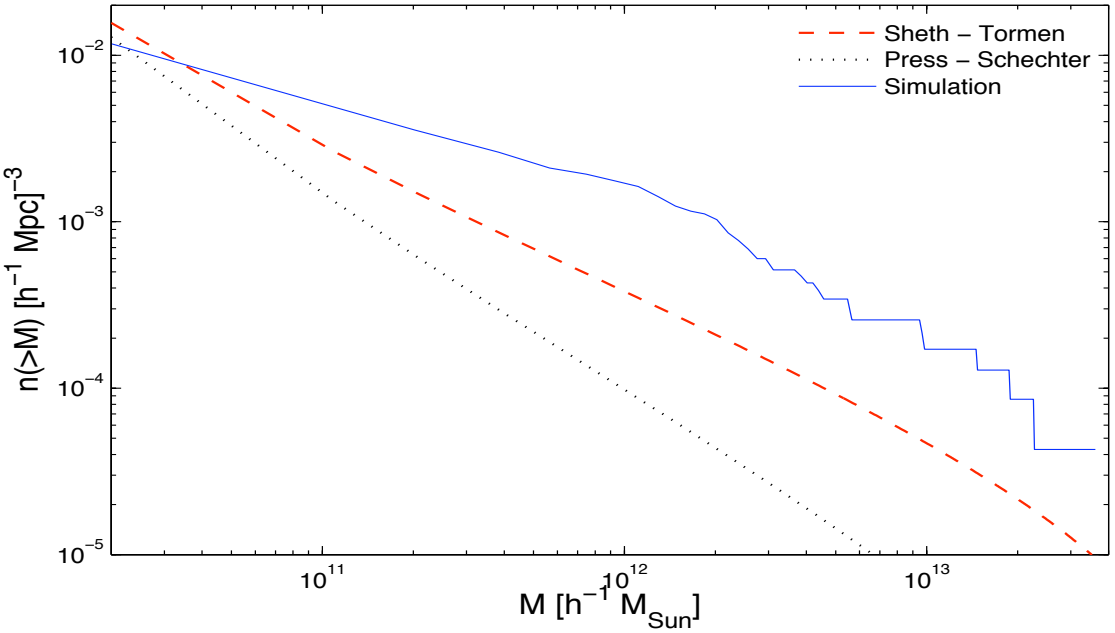

Figure A.1.3: Number density of halos with mass larger than M for $N_{seed} = 2000$. The solid blue line are the halos found by BDM code, while the upper dashed line is the ST approximation and the lower dotted black line is the PS approximation

A.2 Density Profiles

As done in the previous section, the data from the simulation is compared with the theory predictions. Thus, the density profile for the halos is calculated using the model presented by Navarro et al. (1997) (NFW), which is

$$\rho(r) = \frac{\delta_c \rho_c}{x\,(1+x)^2},$$

where $x = r/r_s$, r_s is a scaling radius, ρ_c is the critical density [Eq. (3.1.6)] and δ_c is the critical overdensity defined in the previous section. The value of r_s is given by

$$\left.\frac{d\log\rho(r)}{d\log r}\right|_{r=r_s} = -2.$$

The parameter r_s is determined using the relation

$$M_{vir} \equiv \frac{4\pi}{3}\Delta_{vir}\rho_u r_{vir}^3,$$

where M_{vir} is the virial mass of the halo, ρ_u is the mean density of the Universe and Δ_{vir} is the relation of the density in the halo over the main density ρ_u. In the case of these simulations $\Delta_{vir} \sim 337$. On the other side, the scaling radius comes from $c \equiv r_{vir}/r_s$, being c the concentration, in this case $c = 7$ (Klypin 2000).

The density profile study has been applied for the largest halo found in the results of the BDM code, hence the halo with largest number of particles. The reason of choosing this special case is to avoid as much as possible the discreteness effects due to the lack of particles.

Figs A.2.2, A.2.3 and A.2.4 show the density profile for the three different number of seeds, being the solid blue line the simulated profile and the dashed red line the NFW approximation. It can be seen that the simulated profiles do not agree very well the predictions of NFW, presenting always lower values. Moreover, due to the reduced number of particles, the precision of the profile is very low and discreteness effects appear in form of irregularities and sharp changes of inclination. Thus, even if the general behavior is decreasing, at small radius the profile increase. However, this effect is somehow reduced when higher number of seeds are placed. Furthermore, as the radius increases, therefore more number of particles are included, the difference between the simulation and the values predicted by NFW decrease.

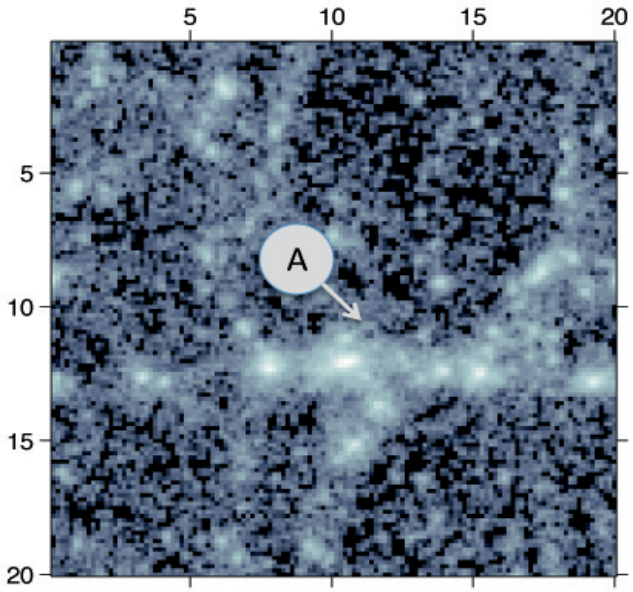

Figure A.2.1: Position of the analyzed halo in the density plot

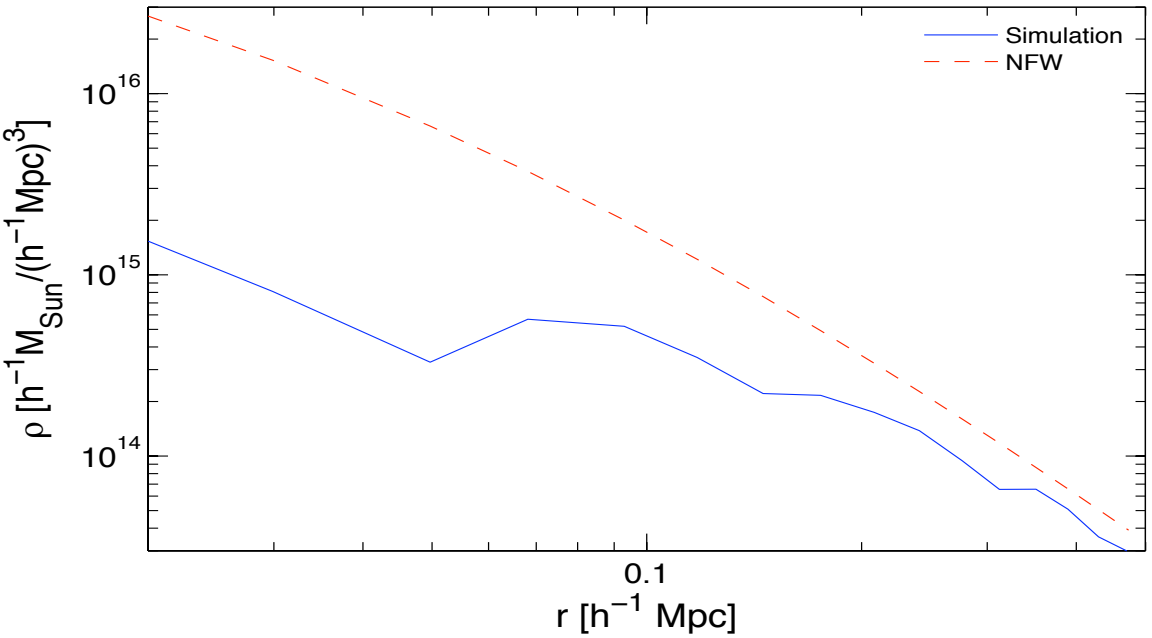

Figure A.2.2: Density profile for the biggest halo for $N_{seed} = 500$. The solid blue represent the simulated profile, while the dashed red line is the NFW approximation

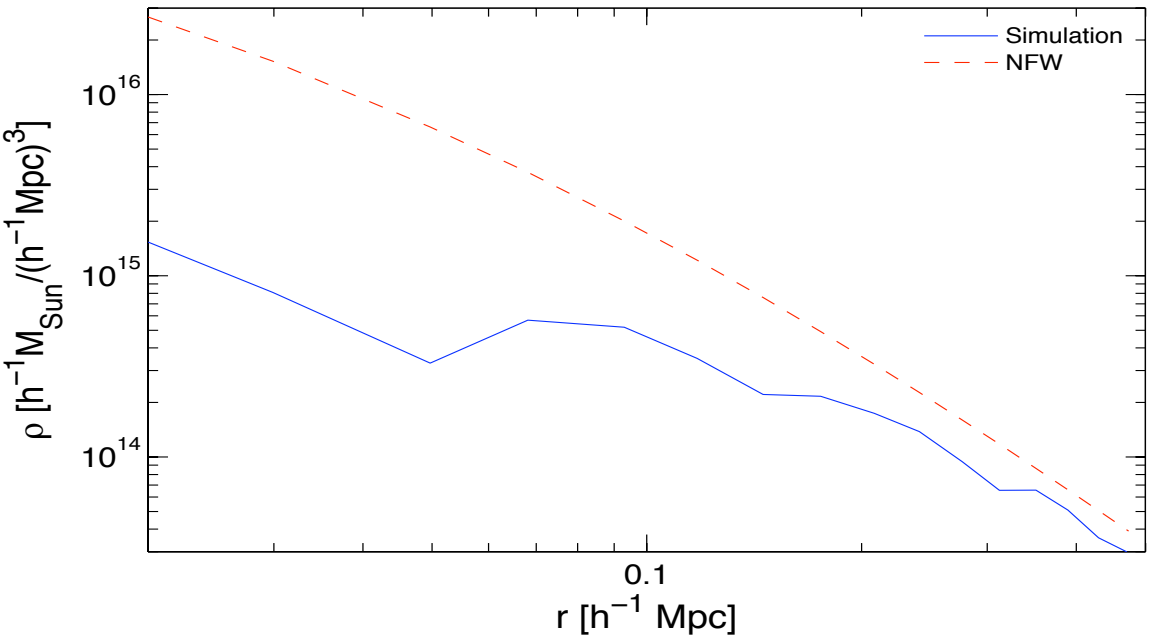

Figure A.2.3: Density profile for the biggest halo for $N_{seed} = 1000$. The solid blue represent the simulated profile, while the dashed red line is the NFW approximation

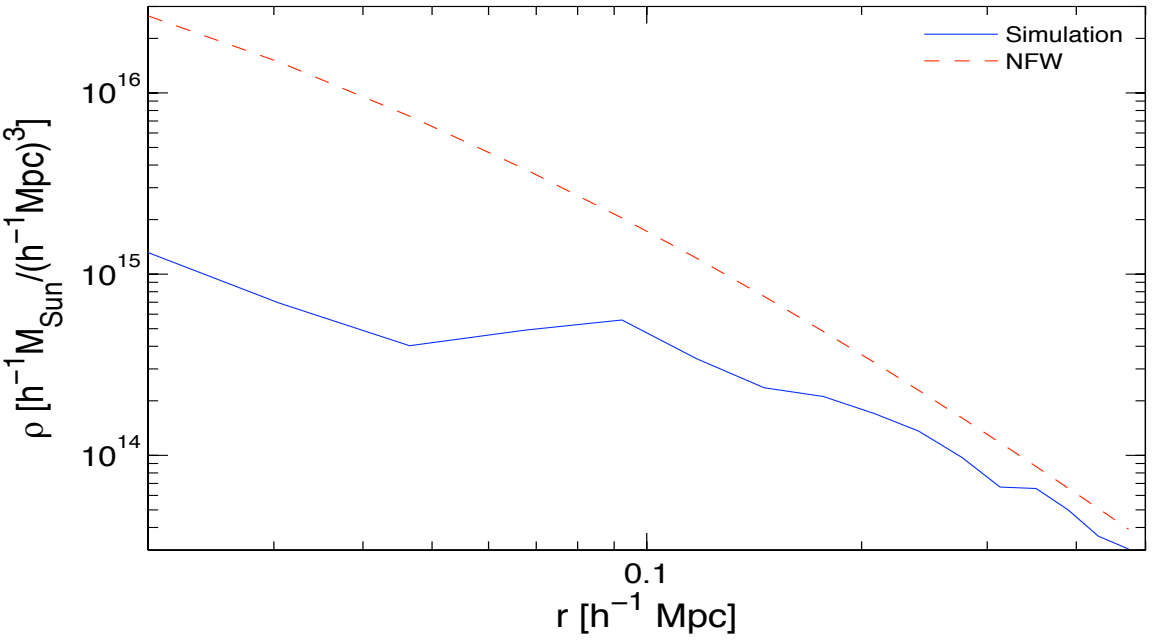

Figure A.2.4: Density profile for the biggest halo for $N_{seed} = 2000$. The solid blue represent the simulated profile, while the dashed red line is the NFW approximation

Appendix B

Quantities of Special Interest in the Code

In this part of the Appendix the equations used for doing the calculations in the thesis are presented, as well as where they can be found inside the simulation code used, the PM code by Klypin & Holtzman (1997). Thus, the FORTRAN program and their exact location is provided in the following list.

B.1 Growth Rate ΛCDM

$\delta_g(a) = \frac{5\Omega_m}{2} H(a) \int_0^a \frac{dx}{(x \cdot H(x))^3}$ `PMmodels.f` : line183, functionAGE

$H(x) = \left[\Omega_m x^{-3} + \Omega_{DE} + (1 - \Omega_m - \Omega_{DE})\, x^{-2}\right]^{1/2}$ `PMmodels.f` : line403

B.2 ΛCDM Linear Power Spectrum

$P_{ini}(k) = \frac{k^n \exp(P_1)}{(1+P_2 k^{1/2}+P_3 k+P_4 k^{3/2}+P_5 k^2)^{2P_6}}$ `PMmodels.f` : line137, functionP(w)

(*)Parameters P_i can be found in the `cdm.fit` file for a range of different cosmologies.

$S_n = \frac{\sigma_8^2}{\int_{10^{-5}}^{20} W(x) dx}$ `PMmodels.f` : line44

$P(k,a) = \left(\frac{Growth factor(a)}{Growth factor(a_0)}\right)^2 P_{ini}(k) \cdot S_n \cdot h^3 (2\pi^2)$ `PMmodels.f` : line86

B.3 HCDM Linear Power Spectrum

$\sigma_8 = \sqrt{\frac{S_n}{\int_{10^{-4}}^{10^{-2}} TopHat + \int_{10^{-2}}^{2\cdot 10^{-1}} TopHat + \int_{2\cdot 10^{-1}}^{2\cdot 10} TopHat}}$ `PMmodelCHDM.f` : line49

$TopHat = \left(\frac{3(\sin x - x \cdot \cos x)}{x^3}\right)^2$ `PMmodelCHDM.f` : line245

$S_n = \frac{Q^2(4\pi)}{2\pi^2 5 \cdot fact(ns,2) \cdot R_h^{(ns+3)}}$ `PMmodelCHDM.f` : line33

$Q = \frac{quadrupole}{2.276\mathrm{K}}$ `PMmodelCHDM.f` : line32

$R_h = \frac{6 \cdot 10^3}{h}$ `PMmodelCHDM.f` : line29

$P_{ini\,cold}(k) = \frac{k}{(1+P_2 k^{1/2}+P_3 k+P_4 k^{3/2}+P_5 k^2)^{2P_6}}$ `PMmodelCHDM.f` : line299

$P_{ini\,hot}(k) = P_{inicold}(k) \frac{k \exp -PP_1 k}{1+PP_2 k^{1/3}+PP_3 k^{2/3}+PP_4 k+PP_5 k^{4/3}+PP_6 k^{5/3}}$ `PMmodelCHDM.f` : line324

(**)Parameters P_i and PP_i are found in PMmodelCHDM.fit in lines 286 and 312.

$P_{COLD}(k,a) = a^2 \Omega_{CDM}^2 P_{inicold}(k) S_n h^3 2\pi^2$ `PMmodelCHDM.f` : line277&74

$P_{HOT}(k,a) = a^2 \Omega_{\nu}^2 P_{inihot}(k) S_n h^3 2\pi^2$ `PMmodelCHDM.f` : line277&74

$P_{lin\,CHDM} = P_{COLD}(k,a) + P_{HOT}(k,a) + 2P_{COLD}(k,a)^{1/2} P_{HOT}(k,a)^{1/2}$